An Investigation on Interfacial Adhesion Energy between Polymeric and Cellulose-Based Additives Embedded in C-S-H Gel

by

Faezeh Shalchy

A Thesis in

Civil and Environmental Engineering Department

Worcester Polytechnic Institute

By

December 2015

Approved:----------- Dr. Leonard Albano:--------------
Dr. Nima Rahbar:----------------- Dr. Tahar Elkorchi:----------------

Abstract

Concrete is one of the most widely used materials in the world. It is also one of the most versatile while complex materials which human have used for construction. However, an important weakness of concrete (cement-based composites) is its weak tensile properties. Therefore, over the past thirty years many studies were focused to improve its tensile properties using a variety of physical and chemical methods. One of the most successful attempts is to use polymer fibers in the structure of concrete to obtain a composite with high tensile strength and ductility. However, a thorough understanding of the mechanical behavior of fiber reinforced concrete requires the knowledge of fiber/matrix interfaces at the nanoscale. In this study, a combination of atomistic simulations and experimental techniques has been used to study the nanostructure of fiber/matrix interfaces. A new model for calcium-silicate-hydrate (C-S-H)/fiber interfaces is also proposed based on Scanning Electron Microscopy (SEM) and Energy-dispersive X-ray spectroscopy (EDX) analyses. Finally, the adhesion energies between the C-S-H gel and three different polymeric fibers (polyvinyl alcohol, nylon-6 and polypropylene) were numerically studied at the atomistic level, since adhesion plays a key role in the design of ductile fiber reinforced composites. The mechanisms of adhesion as a function of the nanostructure of fiber/matrix interfaces are further studied and discussed. It is observed that the functional group in the structure of polymer macromolecule affects the adhesion energy primarily by changing the C/S ratio of the C-S-H at the interface and further by absorbing additional positive ions in the C-S-H structure. Then the mechanical response of cement paste with added polymeric fibers were

i

studied. A correlation between adhesion energies and the load-displacement curve in split-cylinder test was found. Moreover, as there is a great interest in cellulose-based cement composites, bamboo fibers is added to the cement paste and the fiber/matrix interface and its effect on structure of C-S-H were investigated.

Acknowledgment

First and foremost, I want to express my sincerest gratitude to my supervisor, Prof. Nima Rahbar, for his supervision, advice, and guidance throughout the research. I attribute my Master's degree to his encouragement and effort; without him, this thesis would not have been completed or written.

I would like to thank my thesis committee members, Prof. Leonard Albano and Prof. Tahar Elkorchi for their insightful comments and invaluable advice.

I am extraordinarily fortunate in having so many friends during my time at the Worcester Polytechnic Institute. They helped me without any persuasion to complete my Master's degree. Sina Askarinejad, Naser Pourakbar Sharifi, Sina Youssefian and Jessica Rosewitz, thank you all. You are more important to me than you realize.

Finally, I want to show my gratitude to my parents, who sincerely raised me with their caring and gentle love. They may know nothing about my research, but they do always show their support and love all the time throughout my life. Also, I would like to thank everybody who helped me with this thesis, as well as expressing my apology that I could not mention your names personally one by one.

Contents

List of Figures

List of Tables

1. Chapter 1: Fiber/Matrix Interface Characterization by SEM and EDX

1.1. Introduction

As the most used materials in the world, concrete possess excellent compressive strength but weak tensile properties. The cement-based matrix of the concrete has a complex structure that makes concrete a weak material in terms of material properties such as tensile strength and toughness. Therefore, over the past thirty years many studies were focused to improve the tensile properties of concrete (cement-based composites) using a variety of physical and chemical methods [1]-[4]. One of the most successful attempts is to use polymeric materials in the structure of concrete to obtain a composite with high tensile strength and ductility [5]-[8]. Improving the performance of polymer fiber-reinforced cement composites can also increase the durability of concrete structures and decrease the production of carbon dioxide [9; 10]. However, understanding the mechanical behavior of fiber-reinforced concrete requires the thorough knowledge of the fiber/matrix interface structure. While, a large body of microscopic studies have been performed on the interfaces present in fiber-reinforced cement based composites [8; 11; 12], the nanostructure of interfaces between cement and polymer fiber has not been thoroughly investigated. This understanding is needed to fully predict and improve the mechanical properties of fiber-reinforced cement based composites since the fibers change the chemical reactions and chemical productions of hydration reaction. This study presents a combined experimental and numerical study on the nano-structural properties of polymer/cement interfaces. In this chapter, the experimental investigations on the interface struc-

ture is presented using Scanning Electron Microscopy (SEM) and Energy Dispersive X-ray Spectroscopy (EDX).

1.2. SEM and EDX

In this chapter, three polymeric fibers were used to make fiber-reinforced cement paste. Then the interface properties of the fiber and cement paste were investigated. The first two polymer fibers: PVA and nylon-6 with the IUPAC names of polyvinyl alcohol and poly (hexano-6-lactam), respectively, have polar side chains with different polarities. The third polymer fiber is polypropylene, which has a nonpolar side chain. The goal is to observe how the polarity of the side chains affects the nanostructure of fiber/cement interface.

1.2.1. Polymeric Fibers

In this study three different polymer fibers are considered based on the polarities of their side chains. The same functional group usually undergoes the same or similar chemical reaction(s) regardless of the size of its molecule [28]. Nylon-6 has amide groups (see Fig. 1(a)), which have the highest polarities among other functional groups. It has two different high electronegative atoms in its structure: the oxygen, and the nitrogen atoms in the amide group. Both oxygen and nitrogen contribute to hydrogen bonding. Nitrogen atoms are hydrogen bond acceptors and/or donors and oxygen atoms are hydrogen bond acceptor. PVA is one of the most common fibers that have been used in fiber-reinforced cement composites. PVA is from the alcohol group that has hydroxyl side chain (see Fig. 1(b)); On one hand this functional group has less polarity than amide group, on the other hand, the alcoholic functional group has just one oxygen atom that contributes to hydrogen bonding. Oxygen atoms in hydroxyl group are hydrogen bond acceptors and/or donors. The last polymer, polypropylene, is composed of

3

alkanes (Fig. 1(c)). Alkanes have little intermolecular association because the carbon-hydrogen bond is non-polar. Alkanes are essentially non-polar molecules and insoluble in water. All of the fibers were provided by Forta Corporation Company (Grove City, PA).

a) Hexano-6-lactam (Nylon-6)
Molar Mass = 113 g/mole
Molecular Formula : $C_6H_{11}NO$

b) Vinyl-alcohol
Molar Mass= 44 g/mole
Molecular Formula : C_2H_6OH

c) Propylene
Molar Mass= 42 g/mole
Molecular Formula : C_3H_6
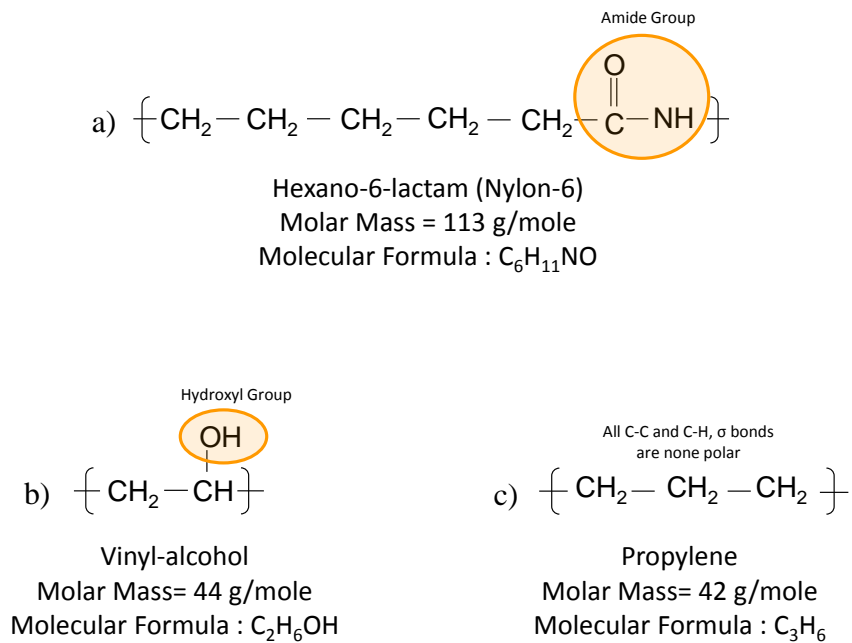
Figure 1: The monomer formula for three different polymers used as fibers in cement paste are shown in this picture: a) monomer for nylon-6, b) monomer of PVA, and c) monomer of polypropylene. It can be observed that nylon-6 has amid side chain on its monomer, while PVA has hydroxyl groups. Polypropylene's macromolecule is mainly non-polar.

4

1.2.2. Fiber-reinforced Samples Preparation

The fiber-reinforced cement paste composites evaluated in this study are prepared by mixing polymer fibers, water and cement powder to obtain mixtures with a specific concentration of fibers for a specific composition of cement. The cement pastes ingredients are mixed with a blender. All samples have 1% volume of polymeric fibers. The following procedure is used for the preparation of the cement pastes: first the weight percentage of cement, fiber, and water are measured in different bowls; then the cement is mixed at a medium speed for 15 s; water and fibers are added to the cement gradually and they are mixed for 90 s. A spatula is used to scrape the wall and bottom of the bowl; Another 90 s of mixing is done at medium speed. After the mixing is complete, the fresh cement pastes are casted in plastic cylinders with 5.1 cm in diameter and 10.2 cm in height, and sealed at 23 ± 1 °C for curing at a curing room. At the age of 24 ± 1 hr, the cylinder samples are demolded. Any excess of moisture on the surface is removed with a towel and the specimens are sealed in plastic bags at 23 ± 1 °C until the age of testing. To ensure desired compressive strength, the samples are tested after 28 days and then are cut using a diamond cutter, and polished to be prepared for the SEM/EDX analysis.

1.3. Results and Discussion

A typical SEM image of the polymer fiber, matrix and polymer/matrix interfacial transition zones for all three types of polymer fibers are shown in Fig. 2. The SEM images of the samples clearly show that there is a transition zone between the polymer fibers and cement paste. These figures show that the interfacial layer between fiber and matrix has a thickness of about 1-5

5

μm around the fiber. Regions of fiber, cement matrix, unhydrated clinkers and fiber/matrix interface are also indicated in the figure. The EDX results and analysis for three different fiber/cement interfaces are shown in Fig. 3. The X-ray mapping is used to investigate the distribution and density of existing elements such as Si, and Ca in an area around each fiber. The X-ray mapping of Si and Ca elements for nylon-6 and PVA fibers clearly show the accumulation of calcium at fiber/matrix interface, which is represented by a circle on the figures. However, this phenomenon is not observed in the samples with nonpolar polypropylene fibers. Moreover, the EDX is performed on ten spectra of the fiber/matrix interface and ten spectra of regular C-S-H gel. The numerical EDX results show that the ratio of C/S in the interfacial zone significantly changes for PVA and nylon-6 fibers, while it remains almost constant for polypropylene fibers, shown in Fig. 4. The ratio of C/S in the interfacial transition zone between PVA and nylon-6 fibers, and cement increases in comparison to the regular C-S-H in fiber-reinforced composite matrices. Furthermore, this ratio does not change for the polypropylene fibers. This can be due to the polarity of different fibers caused by the functional groups on their molecular structure.
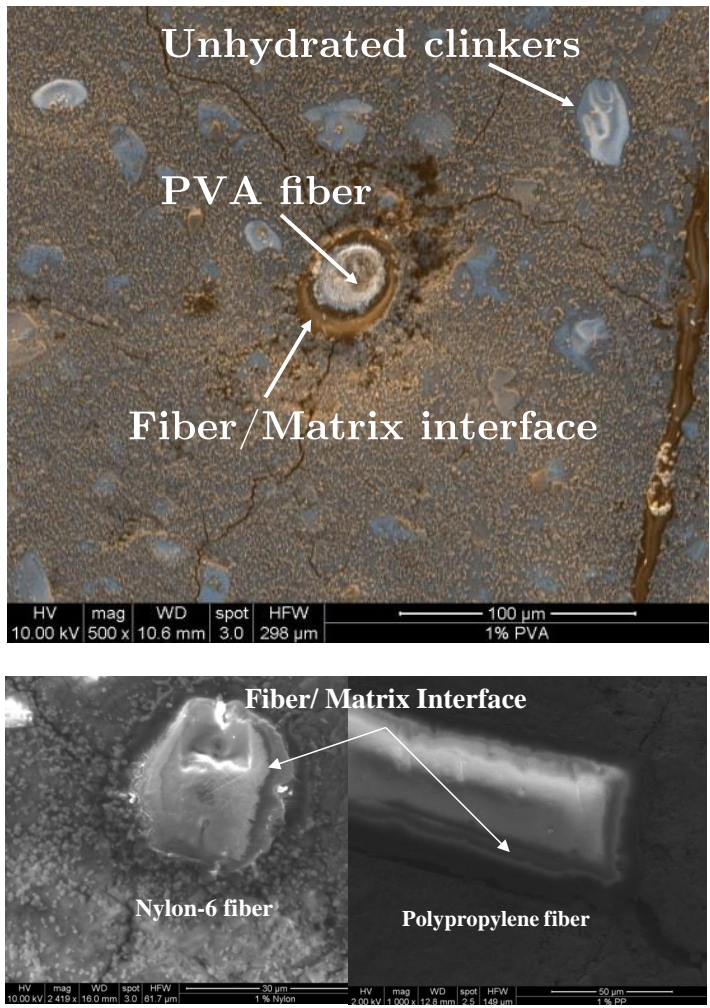
Figure 2: SEM images of fiber/matrix interface for the PVA (top), nylon-6 (bottom left), and polypropylene (bottom right). Regions of fiber/matrix interface are indicated in the image.
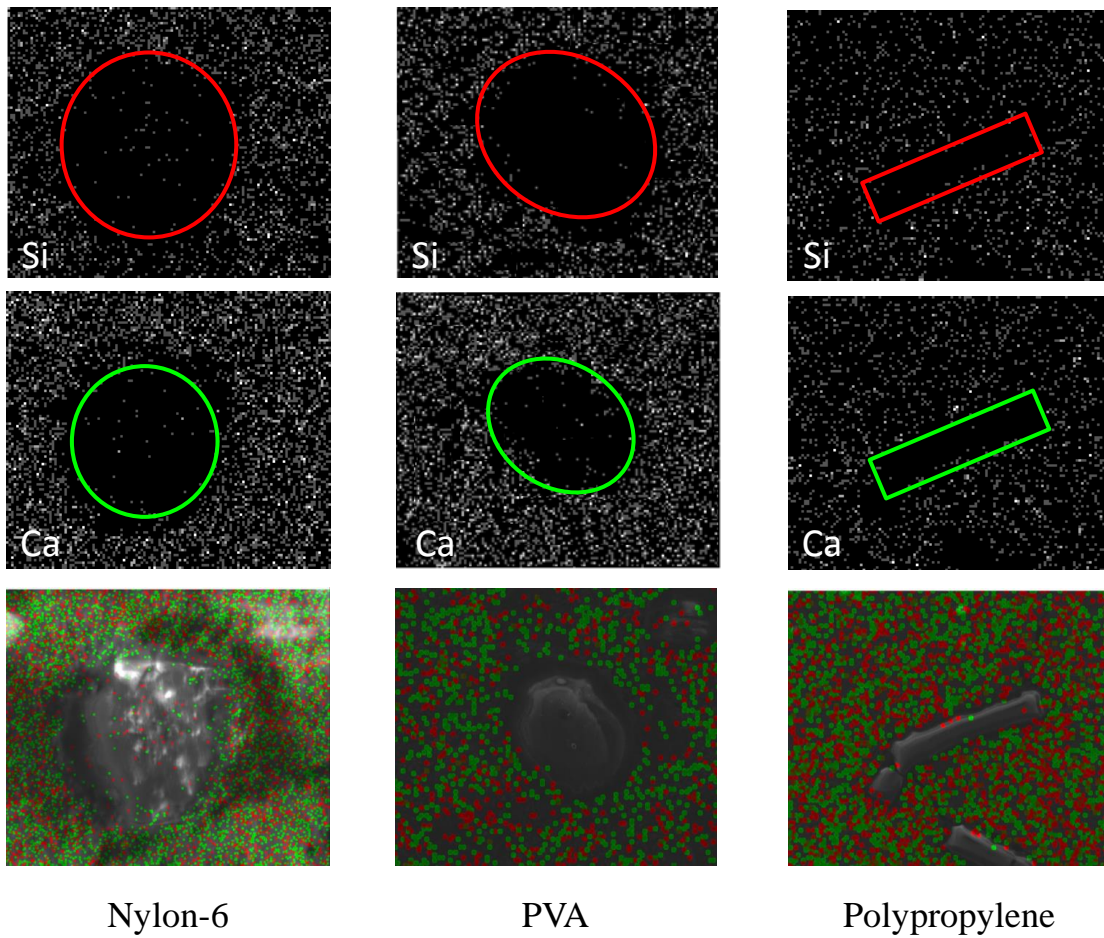
Figure 3: The EDX X-ray map results for three polymeric fibers in C-S-H matrix. The green dots represent Calcium elements and the red dots represent Silicon elements. The results shows that the Ca^{2+} ions are absorbed on the interface of nylon-6 and PVA fibers, but the interface of polypropylene fiber has not significantly changed.
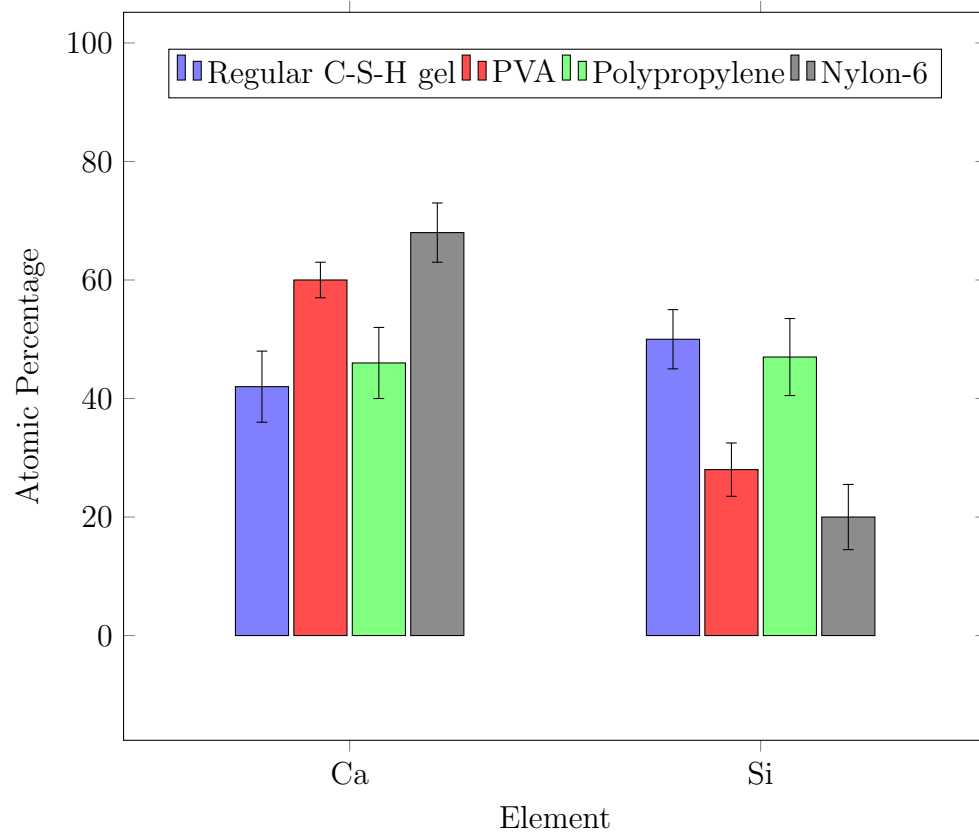
Figure 4: A comparison of the EDX results between atomic percentage of *Ca* and *Si* elements on samples of regular C-S-H gels and EDX results on samples of polymer/C-S-H gel interfaces. Ten EDX spectra are used for each sample.

2. Chapter 2: Molecular Modeling of Concrete

2.1. Introduction

The atomistic structure of the principal hydration product of Portland cement, calcium silicate hydrate, C-S-H (C stands for CaO, S stands for SiO_2 and H stands for H_2O) is first modeled using Molecular Dynamics (MD) and is verified by the available experimental data. In Portland cement, the raw materials are limestone and clay. Hence, a typical composition of a clinker is about 67 % CaO and 22 % SiO_2 with mainly alite (C_3S) and belite (C_2S) molecules. The products of hydration reaction of clinker are mainly portlandite (CH) and C-S-H gel. The C-S-H gel makes up to 70 % of the final volume and is responsible for the cohesion and strong mechanical properties of cement pastes [13].

During the past decade the principal new data bearing on the structure of polymer/cement interface have been on compositions, determined by X-ray microanalysis, and on silicate anion structures [14; 15]. Emphasis is placed on some recent models and their ability to account for these data. There are also many experimental studies on C-S-H gel structure. In a study by Uzun et al. (2011) [15], X-Ray diffraction (XRD) is used to investigate the atomistic structure of C-S-H considering the coordinate number of Ca-O. They believed that C-S-H is an evolution of tobermorite-like structure to jennite-like structure. Allen et al. (2007)[16] measured the mean formula and solid density of the nanoscale C-S-H gel particles by combining small angle neutron and X-Ray scattering data $((CaO)_{1.7}(SiO_2)(H_2O)_{1.8}$ and d=2.604 $\frac{gr}{cm^3})$.

An understanding of the nature of chemical reactions occurring in C-

S-H is also necessary in modeling the mechanical properties of concrete at nanoscale. In order to understand the chemical reactions in C-S-H, many researches have previously tried to characterize the structure of C-S-H gel at the atomistic level [17]-[21]. In that regard, different strategies were utilized to model the atomistic structure of C-S-H in order to understand its nanostructure properties [22; 23]. Bauchy et al. (2014) constructed the tobermorite crystalline structure, a more realistic C-S-H, and an artificial ideal glass [24]. They showed that while C-S-H retains some signatures of a tobermorite-like layered structure, hydrated species are completely amorphous. Earlier, Pellenq et al. (2009) [25] proposed a molecular model for C-S-H gel with the stoichiometry of $(CaO)_{1.65}(SiO_2)(H_2O)_{1.73}$. In a more recent study, Qomi et al. (2014) investigated the effect of C/S ratio on the molecular structure of C-S-H using MD simulation technique [26].

In order to have a better understanding of C-S-H at nanoscale, H. F. W. Taylors postulate is used to begin the atomistic modeling [18]. C-S-H gel is mostly made of Tobermorite and Jennite [24]. Tobermorite has the chemical formulation of $Ca_5Si_6O_{16}(OH)_{2.7}H_2O$ with a C/S ratio of 0.83 and density of 2.18 $\frac{g}{cm^3}$, while Jennite has the chemical formulation of $Ca_9(Si_6O_{18})(OH)_6.8H_2O$ with a C/S ratio of 1.5 and density of 2.27 $\frac{g}{cm^3}$. Moreover, the C/S ratio in C-S-H varies from 0.7 to 2.3 and its density is about 2.6 $\frac{g}{cm^3}$ [20]. Using this information, a more realistic model for C-S-H will be proposed in this chapter.

2.2. Basics of Molecular Modeling

In order to model in molecular level, the position of the atoms and the rules about interaction between them need to be defined.

2.2.1. Forcefield and Simulation Parameters

The selection of a force field that results in an accurate model for the potential energy hypersurface in which the nuclei moves, is an important step in performing atomistic simulations. In general, the potential energy consists of valence, cross-term, and non-bonded energies [29]:

$$E_{total} = E_{valence} + E_{cross-term} + E_{non-bonded} \qquad (1)$$

In Eq. 1, a bond-stretching term, a bending energy term, and four body terms, including a dihedral bond-torsion angle term and an inversion (out-of plane interaction) term have contribution on the valence energy. The cross-term enegy, Ecross-term, accounts for the energy induced by the changes in the bond length and the bond angle with the surrounding atoms. Enon-bonded, the non-bonded term, consists of intermolecular and intramolecular interaction. The non-bonded terms include hydrogen bonds (H-bonds) and van der Waals (vdW) interaction that are the induced dipole-dipole inter-action (also known as London forces). Moreover, the Coulomb interaction accounts for electrostatic interaction. These are summarized in Eq. 2-4.

$$E_{valence} = E_{stretching} + E_{bending} + E_{dihedral-torsion} + E_{inversion} \qquad (2)$$

$$E_{cross-term} = E_{bond-bond} + E_{angle-angle} + E_{bond-angle}$$
$$+ E_{endbond-torsion} + E_{middlebond-torsion} + E_{angle-torsion} + E_{angle-angle-torsion}$$
$$(3)$$

$$E_{non-bonded} = E_{vdW} + E_{coulomb} + E_{H-bond} \qquad (4)$$

12

The COMPASS (condensed-phase optimized molecular potentials for atomistic simulation studies [30]) force field is used for this calculation. It is a powerful force field for atomistic simulation of condensed materials and one of the first ab initio-based force fields that is parameterized and validated with the experiment results [30]. Therefore, it is an accurate and reliable force field for predicting mechanical, structural and thermodynamic properties of vast range of molecules and atoms [31]. It is well parameterized for nonbonded interaction, which makes it a particularly good fit for long-chain molecules like biomaterials or polymers and other systems where the vdW interaction is the governing interaction [32]. Hence, molecular dynamic (MD) simulations are utilized to understand the nanomechanical proprieties of the interface. The unit cell of C-S-H gel and polymer are created and optimized separately. The simulations are performed at room temperature. Hence, the effects of ambient temperature on the structure of interfaces are not studied, since the experiments are done at room temperature after curing. On the other hand, the process of cement hydration is exothermic- it generates heat, but this is during the hydration process in the first 24 hours. Here, the atomistic modeling is performed to simulate the C-S-H/polymer interaction after hydration reaction. In this step, the temperature can be assumed to be constant around room temperature (298 K).

2.3. Cement Paste in Atomic Scale

In this study, the structure of Jennite proposed by Hamid (1980) [17] is used to initiate the basic molecular model of C-S-H. However, in our model, it is assumed that the interlayer Ca^{2+} ions react with water and produce hydroxyl ions. Hence, the structure that is proposed here is made of SiO_2,

Ca^{2+} and Ca(OH)$_2$ layers arranged as shown in Fig. 5. Afterwards, multiple *Si* atoms are randomly omitted from, and multiple Ca^{2+} atoms are added to the structure for the following reasons: 1) to be able to satisfy the C/S ratio in the C-S-H structure at the interface with different polymer fibers, 2) to satisfy the overall charge balance in the system, and 3) to provide the necessary defects in the structure of C-S-H. This approach can be applied to construct different C-S-H models with different C/S ratios using the EDX analysis results. The layered structure of the C-S-H surface is modeled and the potential energy is optimized using the steepest descent approach followed by the conjugate gradient method. The dimensions of the system are 40 Å× 40 Å× 45 Å. The charge distribution is calculated using the QEq method [33]. The non-bonded summations are calculated using Ewald for electrostatic interaction with accuracy of 0.001 $\frac{kcal}{mol}$. Based on each atoms charge with the truncation of atoms further than cut-off distance of 15.5 Å, the charge distribution for van der Waals interaction is computed (Fig. 6).

The thermodynamic properties of the C-S-H are then obtained to assess the suitability of the force field to model the C-S-H gel. The density of C-S-H from the molecular dynamics and experiments are estimated to be about 2.410 $\frac{gr}{cm^3}$ and 2.64 $\frac{gr}{cm^3}$, respectively. The modulus of elasticity is estimated to be 57.02 GPa, 24.52 GPa and 22.20 GPa in X, Y and Z directions (shown in Fig. 6, respectively. Two different methods are used to calculate the elastic moduli. In the first method, the structure is stretched in all three directions and virial stresses are computed. The Youngs moduli is then computed as the average of the three initial stress-strain slopes after relaxation. In the second method, Young's modulus are indirectly computed from molecular
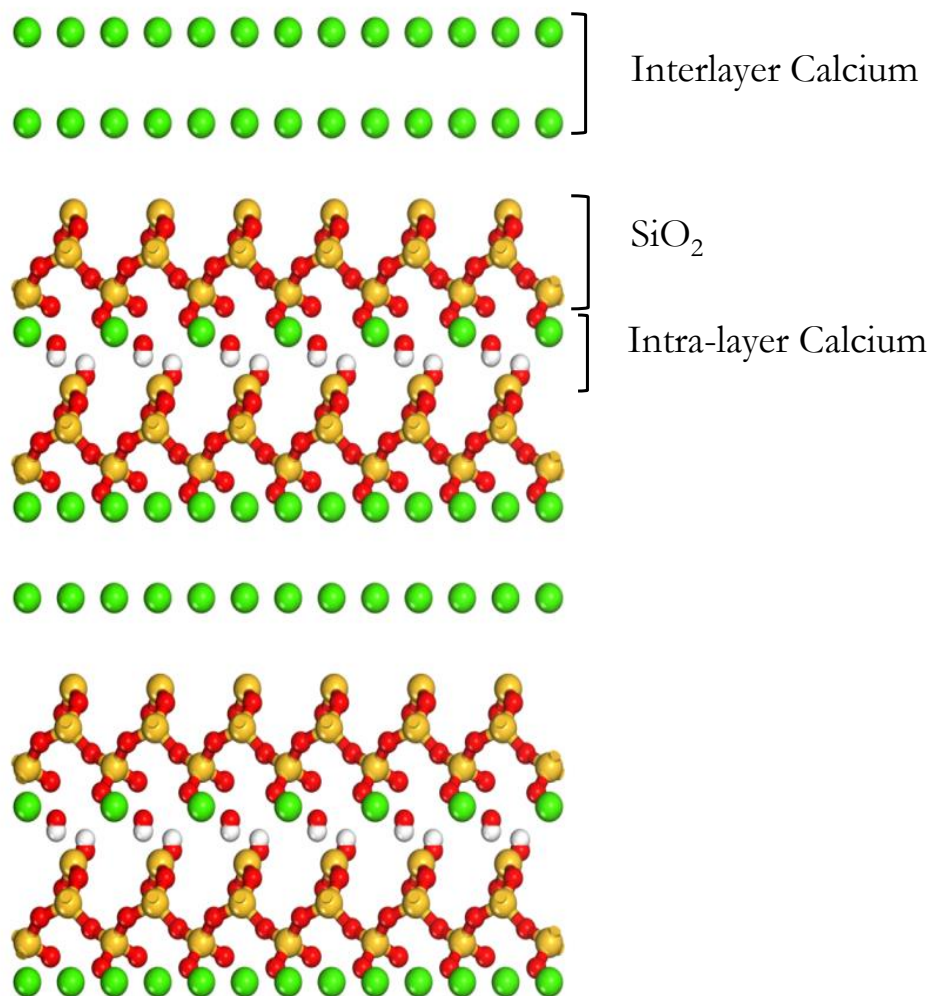
Figure 5: Schematic of the initial molecular model of C-S-H. Red and white spheres are oxygen and hydrogen atoms of water molecules, respectively; the green spheres are calcium ions; yellow and red sticks are silicon and oxygen atoms in silica tetrahedra.
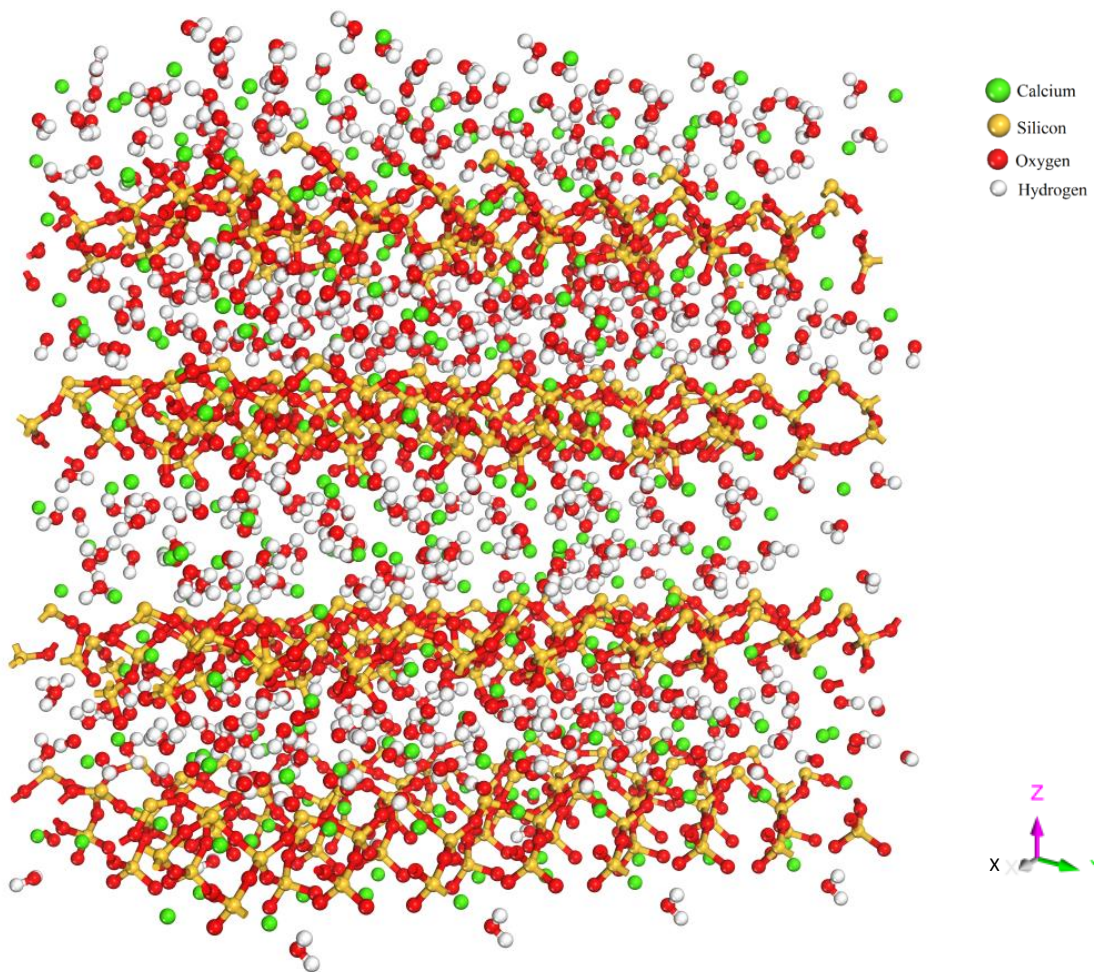
Figure 6: The molecular model of C-S-H after optimization.

dynamic simulation, for each direction, by the following equation:

$$\frac{U}{A \times L} = \frac{E}{2}(\frac{L - L_0}{L_0})$$ (5)

where L_0 is the initial length of unit cell in desired direction. L is the final length and U is the energy of the system after increasing the length. It is observed that both methods result in almost the same value of 32.8 and 34.2 GPa for the suggested C-S-H model. The experimental values corresponding to these properties depend on the volume fraction of the porosities and vary from 30 GPa to 50 GPa [34; 35]. The Poissons ratio of C-S-H is also a function of the volume fraction of porosities and changes from 0.15 to 0.3 [18; 36]. This property is estimated to be 0.29 from the molecular dynamics simulations using the prescribed force field.

3. Chapter 3: Polymeric Fiber Reinforced Concrete: Atomic Scale Properties of Interface

3.1. Introduction

The adhesion energy between fiber and matrix plays a vital role in the mechanical properties of composites [11]. Previously in this study, we have performed SEM and EDX analysis techniques to create a new atomistic model for C-S-H gel and its interface with polymeric materials. The proposed model is studied and analyzed by the molecular dynamic simulation using ab initio-based force fields. The resulting nanostructure of C-S-H using the proposed model is validated by the available Nuclear Magnetic Resonance (NMR) Spectroscopy data. In this chapter, the molecular adhesion mechanisms between a layered structure of C-S-H gel and three different polymeric fibers with a variety of polarities are investigated and the mechanisms of adhesion are reported.

3.2. Molecular Modeling of Polymers

Monomers of the chosen polymers (vinyl alcohol, propylene, and hexano-6-lactam) are constructed and the molecular structures are presented in Fig. 7. Chains of PVA, polypropylene and nylon-6 are then created by assembling 100 monomer units of vinyl alcohol, propylene and hexano-6-lactam, respectively [37].

The structure of the PVA, polypropylene and nylon-6 unit cells are presented in the Fig. 8. The number of monomers in the chain is obviously not representative of the actual polymer chain as the real chain is composed of more than 10,000 repeating units. However, this length is sufficient to model
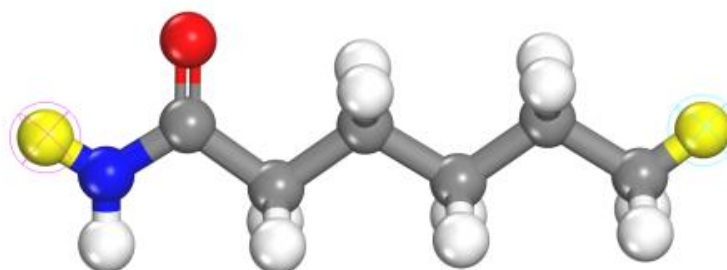
(a) Hexano-6-lactam
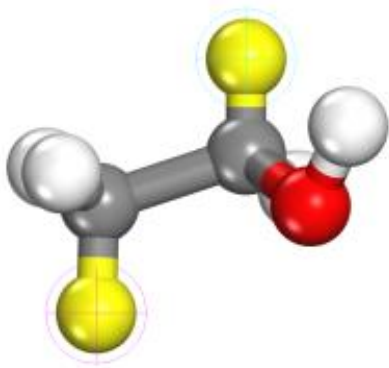
(b) Vinyl-alcohol
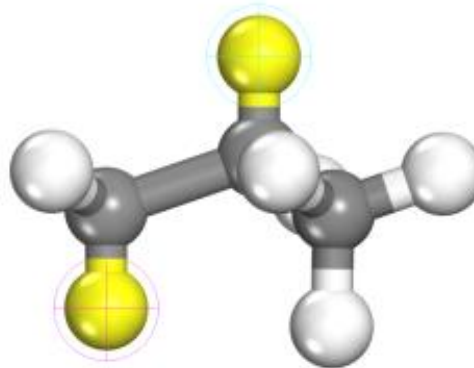
(c) Propylene

Figure 7: Atomistic models of three different polymer atoms investigated in this study. In this figure a, b, and c show the monomer of nylon-6, PVA, and polypropylene, respectively. Gray, red, white, and blue spheres represent carbon, oxygen, hydrogen, and nitrogen, respectively. The yellow atoms show where the monomer is connected to the other monomers in the polymers chain. These locations will be replaced by hydrogen at the beginning and at the end of each chain.

the chain ends, close to the surface. Many monomers on the real chain do not participate in the adhesion process since long-range non-bonded interactions are negligible for these monomers. Chains of 300 monomers and 100 monomers are analyzed and the properties are found to be similar. Hence, for modeling each polymer, 5 chains of 100 monomers are used to simulate the material properties. Additionally, this length is higher than persistent length of these systems. The persistence length of the polymers investigated in this study is roughly around 5-12 nm. This parameter can be estimated using the following equation:

$$P = \frac{B_s}{k_B \times T} \tag{6}$$

where B_s=EI, with E being the Young's Modulus of the polymer, and I=$\frac{r^4}{4}$, r is the radius of molecule's cross section and k_B is the Boltzmann constant. Hence, the persistent length parameter for PVA can be estimated as 7.1 nm. The chain length in our models is around 20 nm, which is more than the persistence length. Moreover, to be able to compute the adhesion energy between C-S-H and the polymers, shorter chains in which the effect of unfolding of chains, intramolecular interactions or self-adhesion can be neglected, are preferable [38]. Five possible structures of each prescribed polymer molecules with desired density of 1.2 $\frac{g}{cm^3}$ at 298 K are created and optimized. Each configuration is subjected to molecular dynamics simulation to let the atoms relax down to the minimum energy in the structure [39]. Initially, the canonical (NVT) dynamics is carried out for 60 ps by 1.0 fs time steps at 300 K, followed by the isothermal-isobaric (NPT) dynamics compressed at high pressure (5000 bar) for 120 ps at 300 K. Next,

20
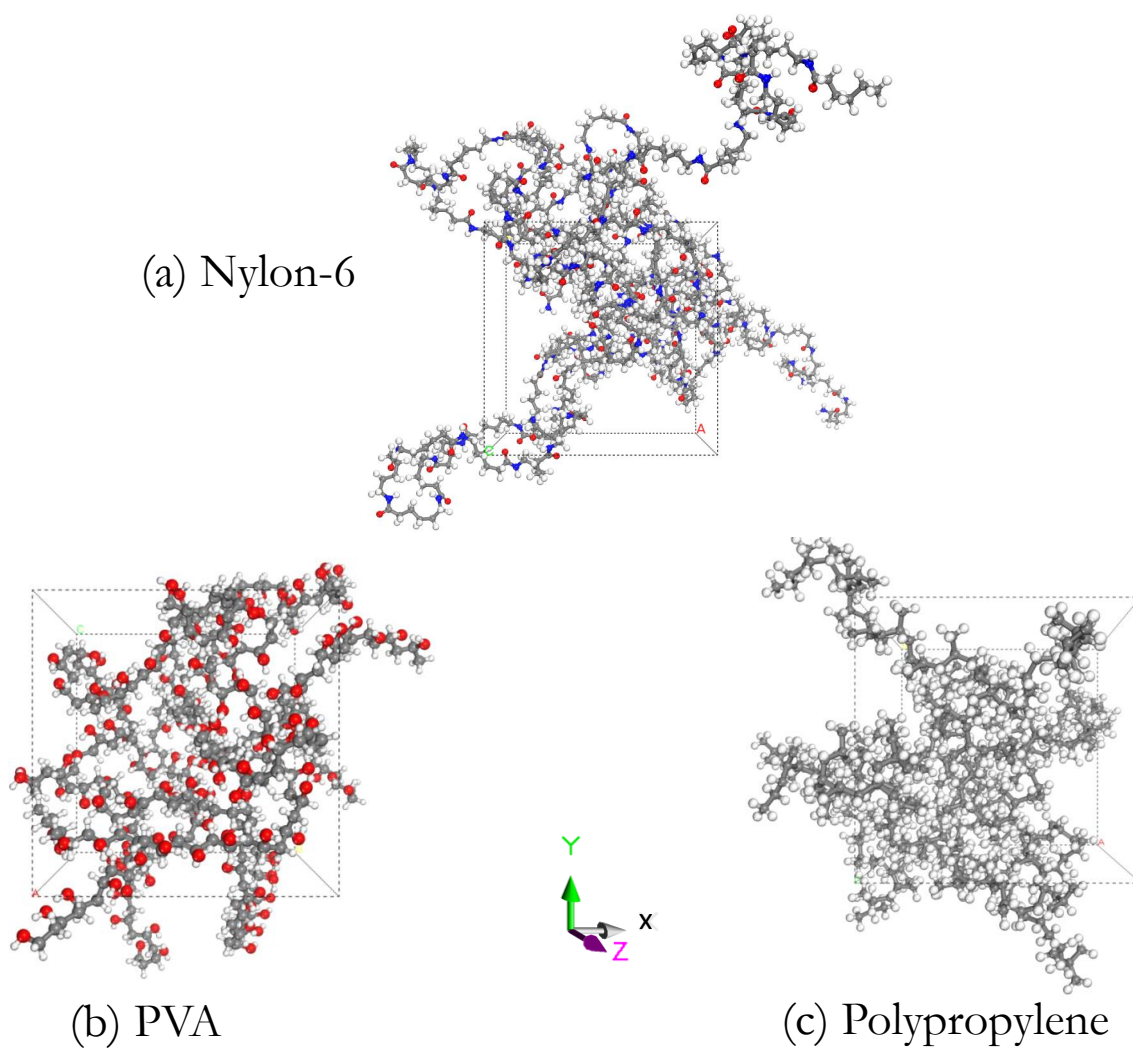
Figure 8: Shows the bulk molecular of nylon-6, PVA and polypropylene models representations in atomistic simulation.

Table 1: Density ($\frac{gr}{cm^3}$) values of PVA, polypropylene, nylon-6 obtained from the atomistic simulations and available experimental data.

Material	Simulation	Experiment
PVA	1.13	1.10 [44]
Polypropylene	0.84	0.952 [45]
Nylon-6	1.10	1.13 [46]

NVT molecular dynamics are applied at 600 K and 300 K, successively, for about 50 ps and 70 ps, respectively. Subsequently, 120 ps molecular dynamics is performed in the NPT ensemble at 1 bar, and the resulting density is compared to the experimental value. If the density is lower than the experimental density, the first two steps are repeated. Finally, molecular dynamics simulation is performed in NVT ensemble at 1 bar for 300 ps. The simulation results of the density for each polymer are presented in Table 1. The computed densities are close to available experimental data. Additionally, in order to verify the structure of the polymers, the convergence of Root Mean Square Deviations (RMSD)s is also checked.

Young's modulus is a measure of the stiffness of an elastic material. Using molecular dynamics simulations, this parameter is found by equation 5 for each polymer. Young's moduli of the PVA, polypropylene, and nylon-6 computed from the stiffness matrices, are presented in Table 2. The average Young's moduli of polymers are in a good agreement with the respective experimental measurements.

The glass transition temperature (T_g) is the reversible transition in amorphous materials from a hard and relatively brittle state into a molten or

Table 2: Youngs Moduli (GPa) of PVA, polypropylene, nylon-6 obtained from the atomistic simulations and available experimental data

Material	Simulation	Experiment
PVA	1.47	2-4 [47]
Polypropylene	2.42	1.1-1.5 [48]
Nylon-6	3.72	1.2-2.8 [49; 50]

rubber-like state. From a thermodynamic point of view, the glass transition temperature appears as a change in the slope of the specific volume and energy versus temperature [40]. The glass transition temperature (T_g) is obtained from the change in the slope of specific energy-temperature curve [39; 41]. To achieve this, the temperature of each system is increased to 600 K and slowly brought down to 200 K at the rate of 0.5 K/ps while the temperature and pressure are controlled by the Nose thermostat and Berendsen barostat, respectively. In random steps, the system is equilibrated with NPT dynamics for 25 ps and the results are recorded to create the specific energy-temperature curves. The variation of the specific energy with temperature for nylon-6 is presented in the Fig. 9. As expected, linear variations are observed on both sides of a critical temperature. This critical temperature should correspond to the glass transition temperature.

The glass transition temperatures of nylon-6, PVA, and polypropylene are computed and compared with the experimental results in Table 3. The small difference between experimental and simulation result is due to the fact that this value will strongly depend on the time scale at which the measurements are performed.
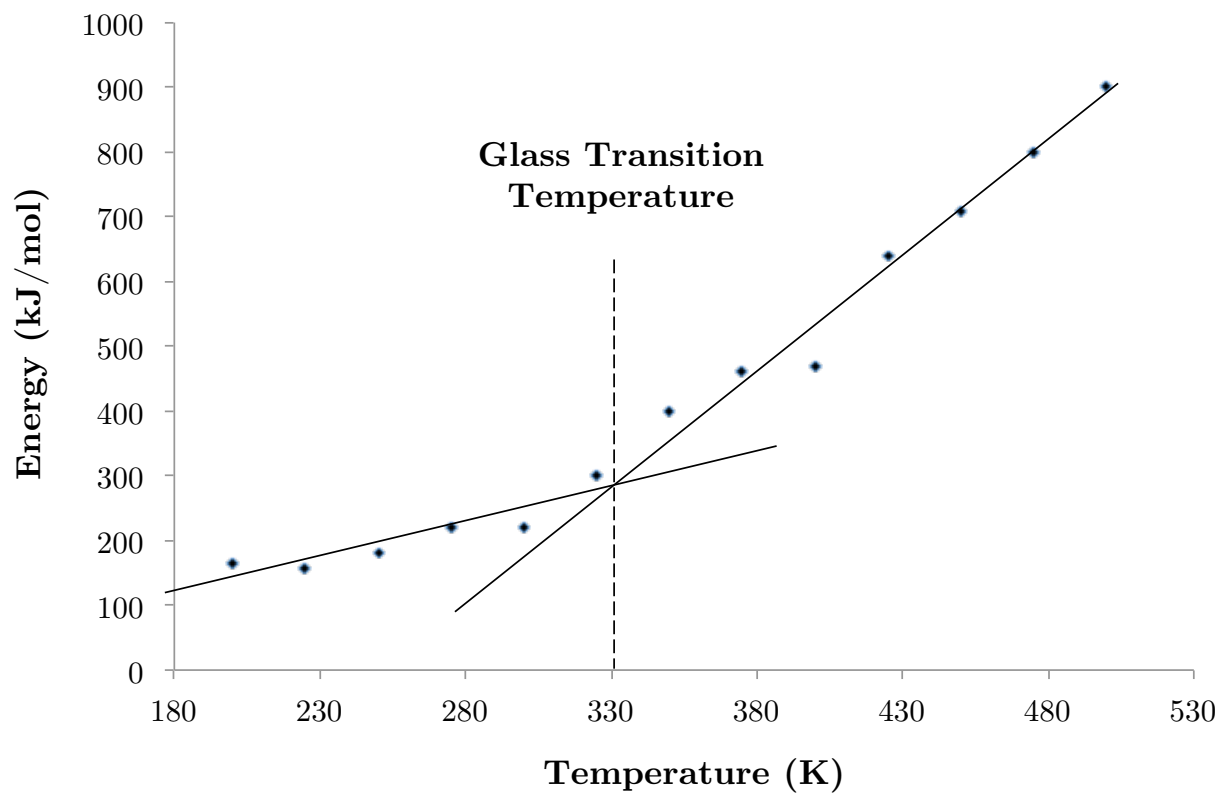
Figure 9: The variation of the specific energy as a function of temperature for nylon-6 is presented. The glass transition temperature is obtained from the change in the slope of specific energy-temperature curve. To achieve this, the temperature of each system is increased to 600 K and slowly brought down to 200 K at the rate of 0.5 K/ps while the temperature and pressure are controlled by the Nose thermostat and Berendsen barostat, respectively.

Table 3: Glass transition temperatures (°C) of PVA, polypropylene, nylon-6 obtained from the atomistic simulations and available experimental data

Material	Simulation	Experiment
PVA	92.4	87 [51]
Polypropylene	16.7	20-25 [44]
Nylon-6	58.1	49 [44]

3.3. Atomic Interaction and Adhesion Energy

To measure the adhesion energies between the polymers and C-S-H gel, models are constructed by placing polymer chains on the C-S-H surface models in a super-cell. When the polymer is placed on top of the layered structure, the polymer will be able to see both sides of the surface due to periodic boundary conditions. Therefore, a large vacuum (50 Å) should be added above the polymer so that it can interact only with one side of the surface. Five different configurations of each chain of polymer are chosen as a confined layer on top of the C-S-H gel. Then, the polymer layers are positioned on the top of C-S-H layer and the whole system is optimized to compute the minimum energy of the system. This is followed by the molecular dynamic simulation of the system under NVT ensemble at the temperature of 298 K for a period of 1 ps. The presence of Ca^{2+} ions makes the system positively charged. Therefore, we have used the QEq method [33] to redistribute the overall charge on the atoms in the current atomistic model. After energy optimization of the cell, 120 ps of dynamic simulations with 1 fs time steps are performed. This time period is enough for the systems to reach the convergence and energy stability. In this dynamic simulation, the charge is set

to zero to eliminate the effect of charges resulting from the Ca^{2+} ions. Furthermore, in order to eliminate the effect of temperature on the adhesion, the simulations are performed at room temperature. Polymers behave differently under different solvation conditions, especially in terms of the ions present in the system. However, the representative polymer systems studied here have no explicit solvent.

3.3.1. Cement Paste in the Interface

The complex atomistic model of C-S-H gel can be verified by important stoichiometric parameter such as C/S ratio, and the first and second order thermodynamic quantities, such as density and Young's modulus. All these parameters were explored in the previous section and their agreement with the experimental model were confirmed. Another important factor that needs to be verified with available experimental data to make sure that the atomistic model is representative of the actual molecules is the Radial Distribution function (RDF). In a solid, the radial distribution function has an infinite number of sharp peaks whose separations and heights are characteristic of the lattice structure. The radial distribution functions of O-H, O-Ca, O-O, Si-Si, Ca-Ca, and Ca-Si pairs are shown in Fig. 10. These results match precisely with the earlier NMR investigated RDF graphs of C-S-H by Lequeux (1999) [42]. After verification of the model by the agreement between the presented parameters in our model and experimental data, the adhesion energies between the C-S-H model and PVA, polypropylene, and nylon-6 polymer fiber surface are investigated.
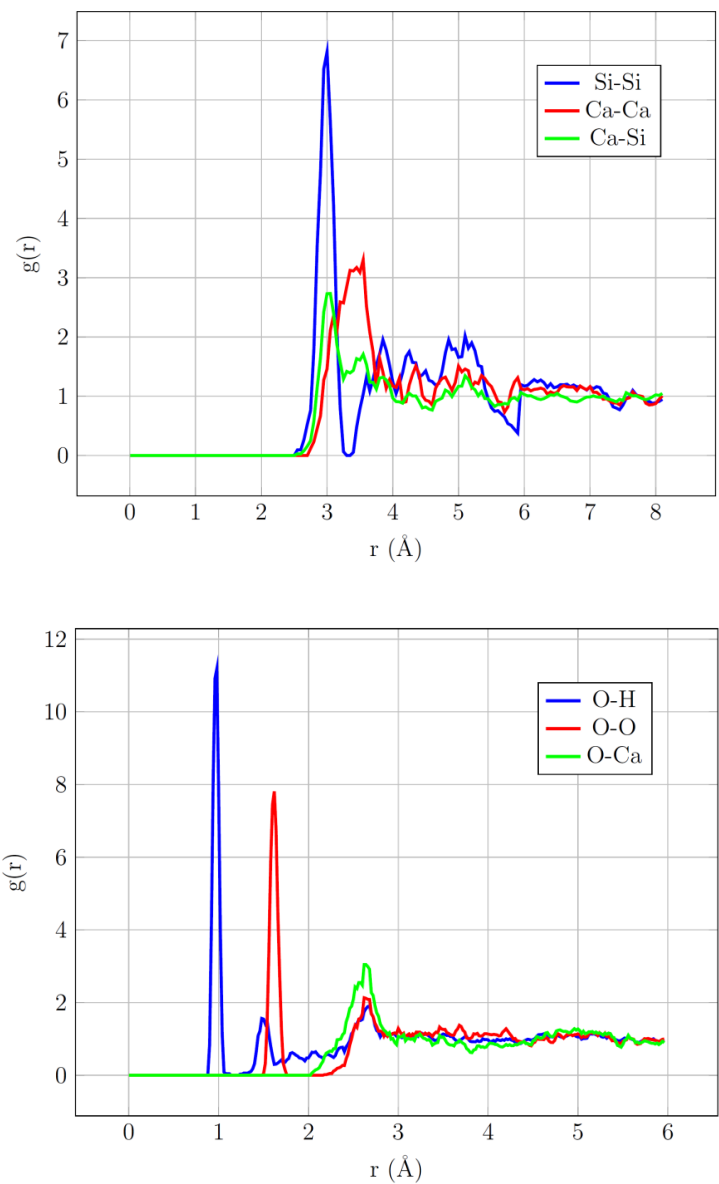
Figure 10: Radial distribution function of Si-Si, Ca-Ca, Ca-Si pairs (top) and O-O, O-Ca, O-H pairs (bottom) in C-S-H gel pairs in C-S-H gel.

3.3.2. C-S-H/Polymer Interaction

The snapshots of the C-S-H/polymer model before and after the MD simulation for nylon-6, PVA and polypropylene interfaces are shown in Figs. 11, 12 and 13, respectively. The binding energies between the C-S-H and polymers and the concentration profiles of the specific atoms are calculated after the MD simulations.

The interaction energy ($E_{Interaction}$) between the polymer molecules and the C-S-H surface is calculated by using the following equation:

$$E_{Interaction} = (E_{C-S-H} + E_{polymer}) - E_{total} \qquad (7)$$

where $E_{Interaction}$ is the interaction energy of the system. E_{total} is the total energy of the C-S-H surface and the polymer molecules in equilibrium. E_{C-S-H} is the energy of the surface without the polymer, and $E_{polymer}$ is the energy of the polymer without the surface, both separated in vacuum in equilibrium [43]. These calculations are all single point energies with no constraints defined in the model.

To investigate the effect of polarity of fibers and C/S ratio, on the adhesion energy of the fiber and cement, various atomistic simulation models are performed. The results of the simulations for nylon-6, PVA and polypropylene interfaces with C-S-H gel are presented in Figs. 11, 12 and 13, respectively. The accumulation of Ca^{2+} ions at the interface of nylon-6 and PVA can be observed in Fig. 11 and 12, respectively. In order to understand the effect of C/S ratio at the interface of C-S-H on the adhesion energy, the adhesion energy between C-S-H models with different C/S ratios with PVA fibers are investigated, and the results are presented in Fig. 14. These results clearly show that higher C/S ratios in C-S-H gel result in higher adhesion
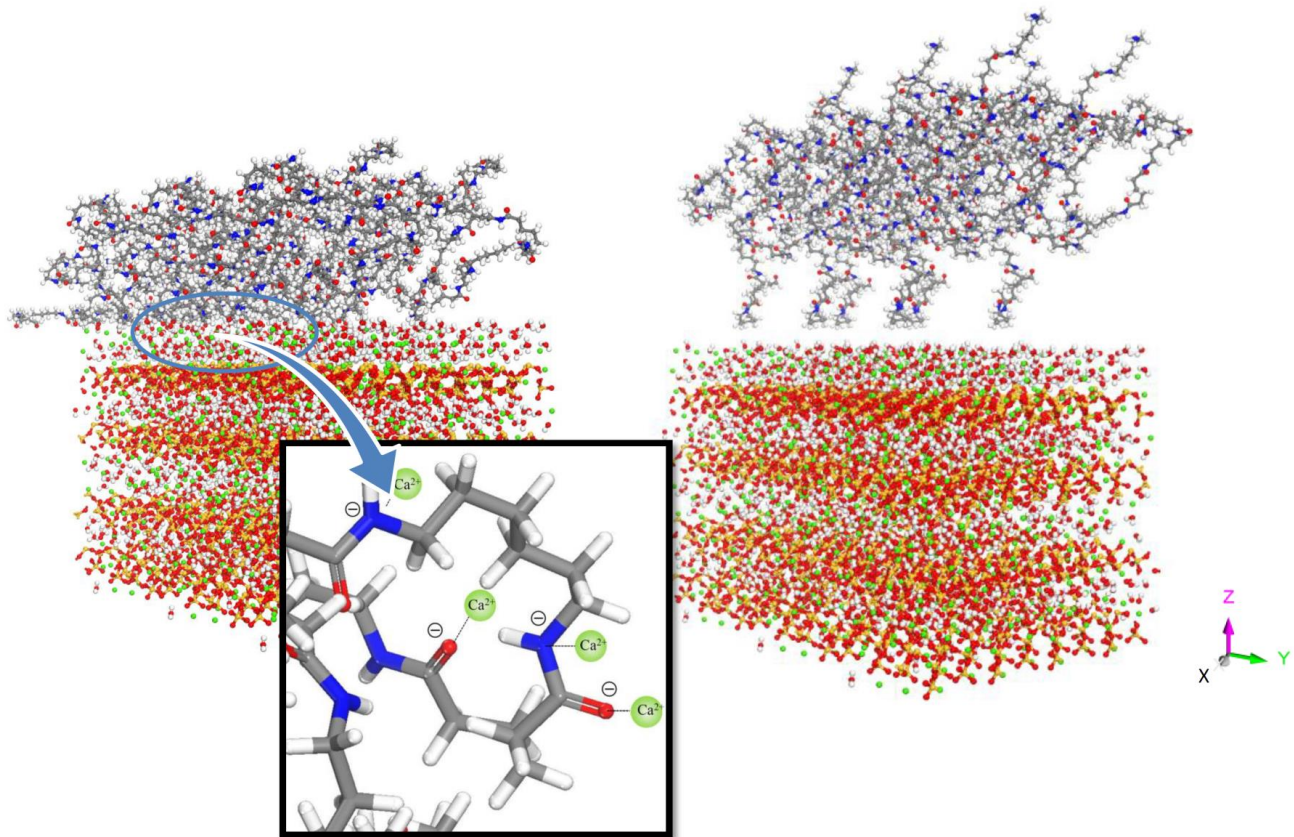
Figure 11: The nanostructure of nylon-6/C-S-H interface before, (right), and after simulation (left).
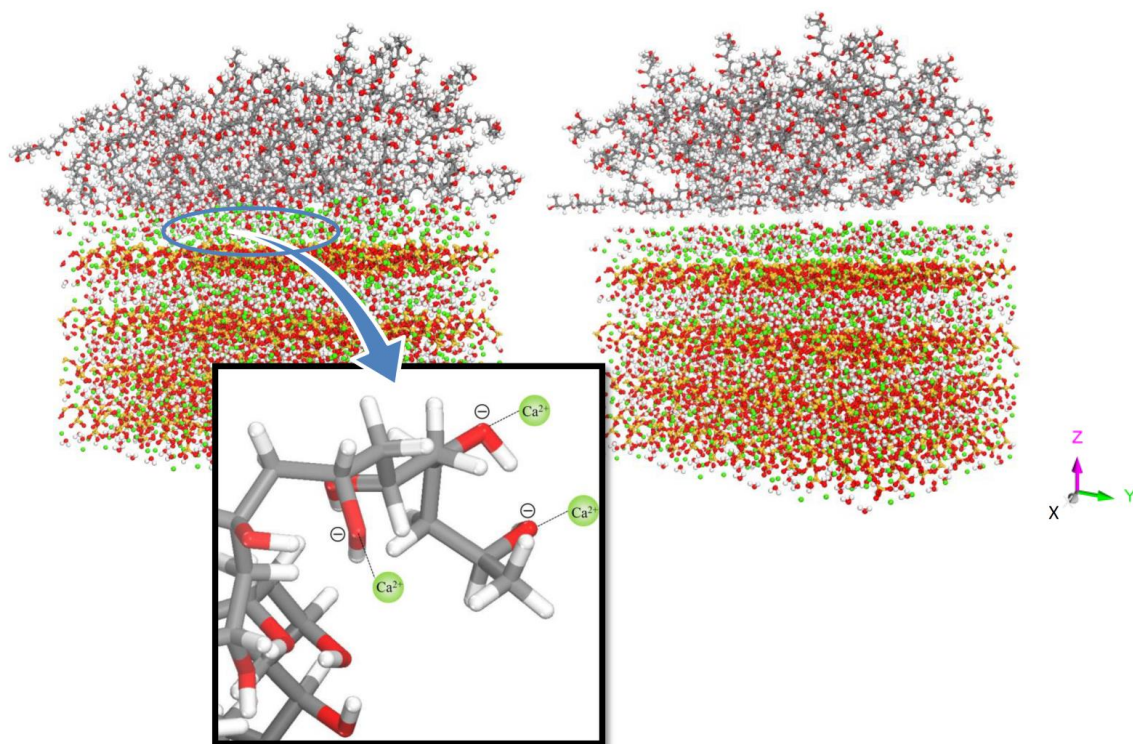
Figure 12: The nanostructure of PVA/C-S-H interface before, (right), and after simulation (left).
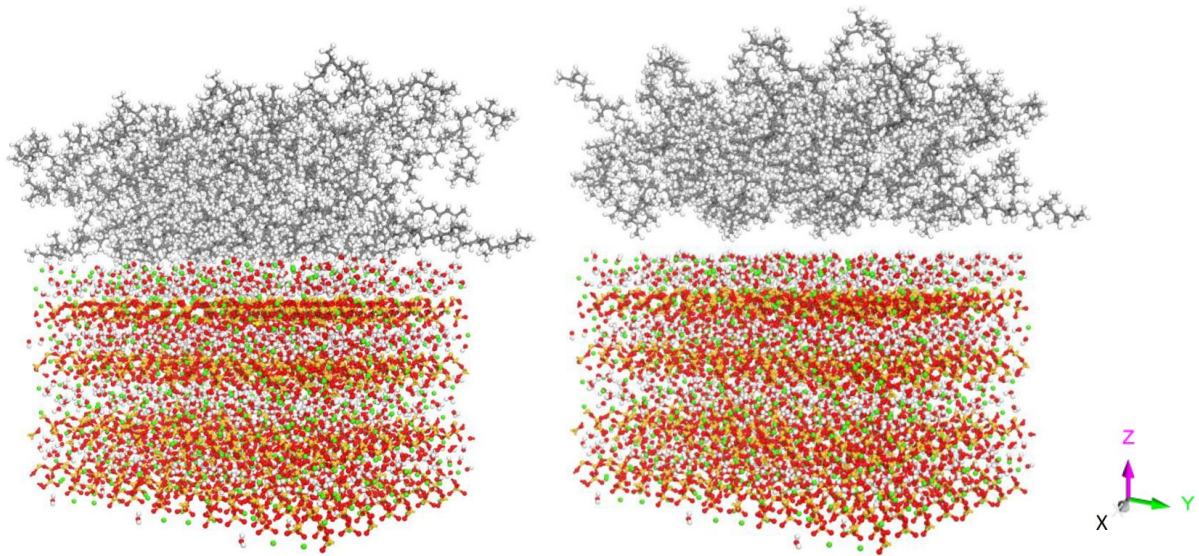
Figure 13: The nanostructure of polypropylene/C-S-H interface before, (right), and after simulation (left).

energies with PVA. This is mainly due to the existence of extra Ca^{2+} ions that make the electrostatic bond with the hydroxyl group of the fibers. This electrostatic bond is the origin of adhesion energy.
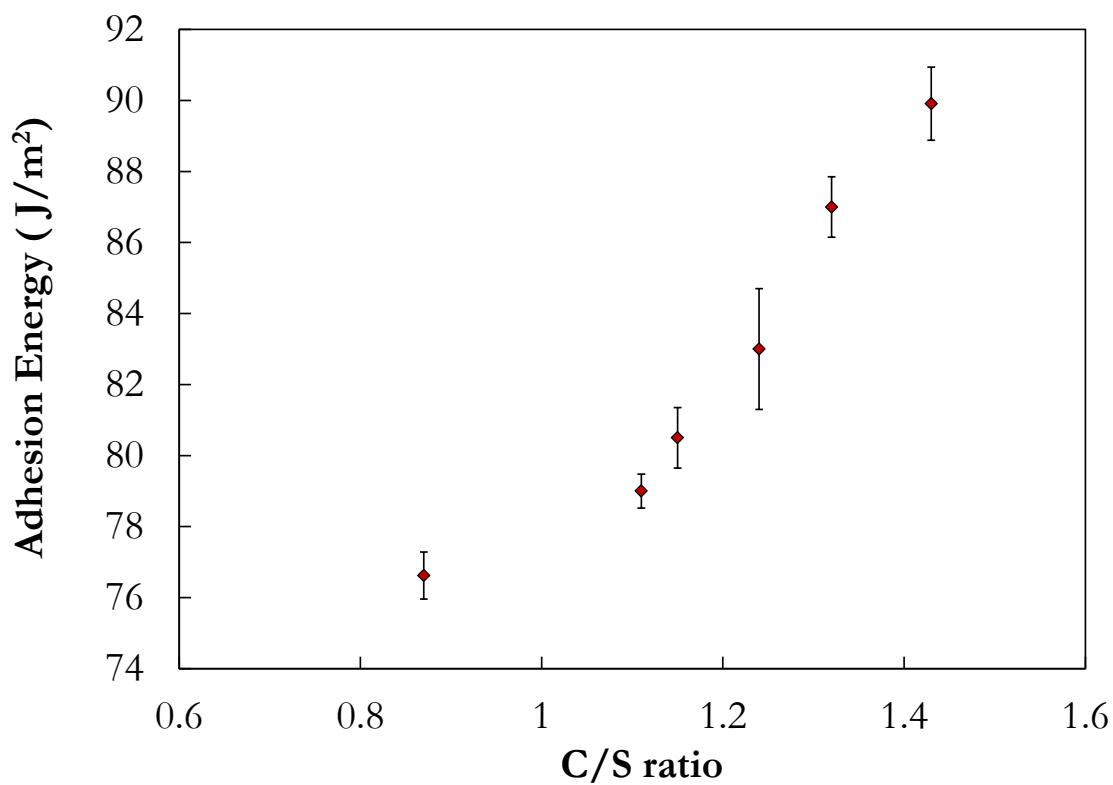
Figure 14: Adhesion energies between PVA fiber and C-S-H gel as a function of interface C/S ratio.

To understand the effect of polarity on the adhesion of matrix and fiber, the adhesion energies between the polymers and C-S-H model, with different C/S ratios of 0.87, 1.24, and 1.43 are computed and are presented in Fig.
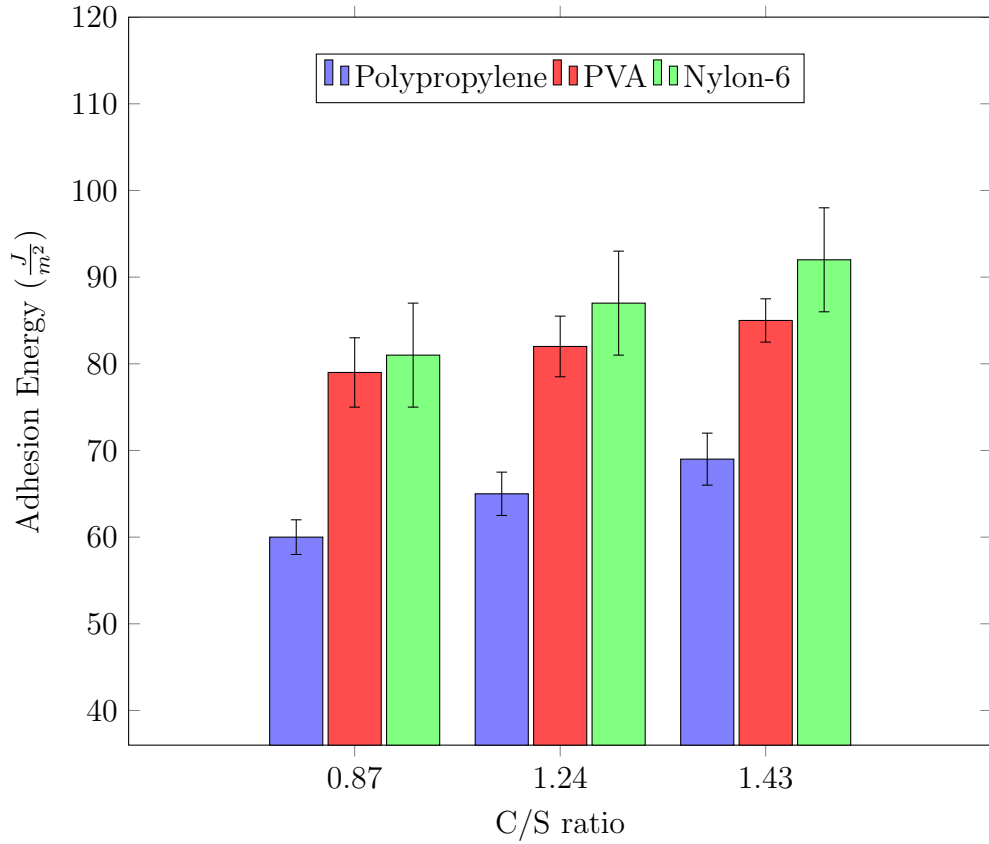
Figure 15: Adhesion energies between polymers with different polarities with C-S-H as a function of interface C/S ratio.

15. The results show that the adhesion energy increases as the polarity of the functional groups increases for each C/S ratio. The amide group is a high polarity group having both oxygen and nitrogen sides in the functional group that can make hydrogen bonds, and moreover interact with Ca^{2+}. The hydroxyl functional group has a moderate polarity with one side that can interact with Ca^{2+} ion. Lastly, polypropylene does not have a polar functional group.

Table 4: The contribution of hydrogen bonding, electrostatic and van der Waals interaction energies ($\frac{J}{m^2}$) to the total adhesion energy ($\frac{J}{m^2}$) between polymers and C-S-H gel.

Adhesion Energy	Total	Hydrogen Bond	Van der Waals	Electrostatic
PVA	89.91	0.58	18.34	71.00
Polypropylene	64.18	0.02	0.24	63.92
Nylon-6	95.48	3.24	13.87	78.38

As it is shown in EDX analysis, the C/S ratio in C-S-H gel increases for polymer fiber reinforced concrete interfaces with polar fibers. The polarity of polymer fibers enhances the absorption of water molecules and the positive ions, such as Ca^{2+} solved in it during hardening to the fiber molecules. Hence, the more realistic adhesion energy for each type of fiber reinforced concrete can be calculated using the actual C/S ratio in C-S-H gel. The final interaction energies and the computed adhesion energies between PVA, polypropylene, and nylon-6, and relevant C-S-H gel model are presented in Table 4. Adhesion energy between PVA, polypropylene and nylon-6 and C-S-H gel are computed as 89.91 $\frac{kJ}{m^2}$, 95.48 $\frac{kJ}{m^2}$, and 64.18 $\frac{kJ}{m^2}$, respectively. The variation in the computed adhesion energies is due to the presence of functional groups, and hence, different polarities of the polymer molecules. We believe that the functional groups affect the adhesion energy primarily by changing the C/S ratio of the C-S-H at the interface, and further by absorbing additional positive ions in the C-S-H structure.

The contribution of hydrogen bonding, electrostatic and van der Waals interaction energies to the total energy in the system are presented in Table 4. The results show that the adhesion energy between fibers and C-S-H gel is mostly a result of electrostatic interaction, which is due to the presence

34

of Ca^{2+} ions in C-S-H model. However, their strength increases with the induced polarity of the polymers. Additionally, the origin of the differences in the van der Waals bond strength is the permanent polarity of PVA and nylon-6 molecules. The difference in the hydrogen bond strength between C-S-H gel and fibers is that in the nylon-6 molecules both oxygen and nitrogen atoms contribute to the hydrogen bonding, while in PVA molecules only one oxygen atom contributes to the hydrogen bonding, while none of them exists in the polypropylene molecule to add to the adhesion energy.

4. Chapter 4: Cellulose as an Additive to Concrete

4.1. Introduction

Products made from renewable and sustainable resources that are biodegradable, non-petroleum based, carbon neutral, and have low environmental, animal/human health and safety risks are increasingly demanded by consumers, industry, and government. Wood, bamboo and cotton have been used by our society as engineering materials for thousands of years and their use continues today as verified by the enormity of the world wide industries in forest products, paper, textiles, etc. These natural materials are mainly made of cellulose. Cellulose is the most abundant naturally occurring polymer, has been the target of great interest in recent years. Cellulose-based biocomposites offer the potential to replace petroleum-based plastics and composites.[52; 53] Hence, investigating the properties of cellulose and its interaction with other materials is an essential to improve the products which contain wood, bamboo or cotton.

These materials were used in the last decades to satisfy the demands using their outstanding properties such as functionality, flexibility and high mechanical strength/weight performance by exploiting hierarchical structure design that spans nanoscale to macroscopic dimensions. However, more multiscale analysis needs to be performed for the advanced next generation materials with special applications. Cellulose nanoparticles is the base fundamental reinforcement unit that is used to strengthen all subsequent structures within trees, plants, some marine creatures, and algae. Extracting cellulose nano-particles allows us to fabricate high performance composites and enhance the mechanical properties of materials such as concrete.

4.2. Molecular Modeling of Cellulose

Molecular dynamics computer simulation has been shown to be an excellent tool to contribute to a molecular-level under standing of crystalline cellulose, its structure and its dynamics, as well as its interactions with solvents and other biomolecules. [54]-[58] At present, there exist several force fields that are being used in simulations of cellulose, such as GROMOS 45a4, [59] CHARMM36,[60] PCFF,[61] and GLYCAM06,[62] to mention a few. These are all atomistic force fields, meaning that all atoms, except for nonpolar hydrogen atoms in the case of GROMOS, are represented explicitly by one interaction site, making the simulations limited to fairly small systems and short simulation times. In our study COMPASS forcefield is used to model cellulose.

Cellulose is a linear chain of ringed glucose molecules and has a flat ribbon-like conformation. The repeat unit (Fig. 16) is comprised of two anhydroglucose rings $((C_6H_{10}O_5)_n$; n = 10,000 to 15,000, where n is depended on the cellulose source material) linked together through an oxygen covalently bonded to the rings. Monomer of cellulose (glucose) is constructed and the molecular structures are presented in Fig. 17.

The structure of natural wood is around 50 % made of cellulose. Wood cellulose is mostly crystalline, however some part of it is amorphous. In this study both crystalline and noncrystalline cellulose are modeled.

In order to model noncrystalline cellulose, chains of cellulose are then created by assembling 100 monomer units of glucose [37]. The structure of cellulose unit cell is presented in Fig. 18. The number of monomers in the chain is obviously not representative of the actual polymer chain as the real
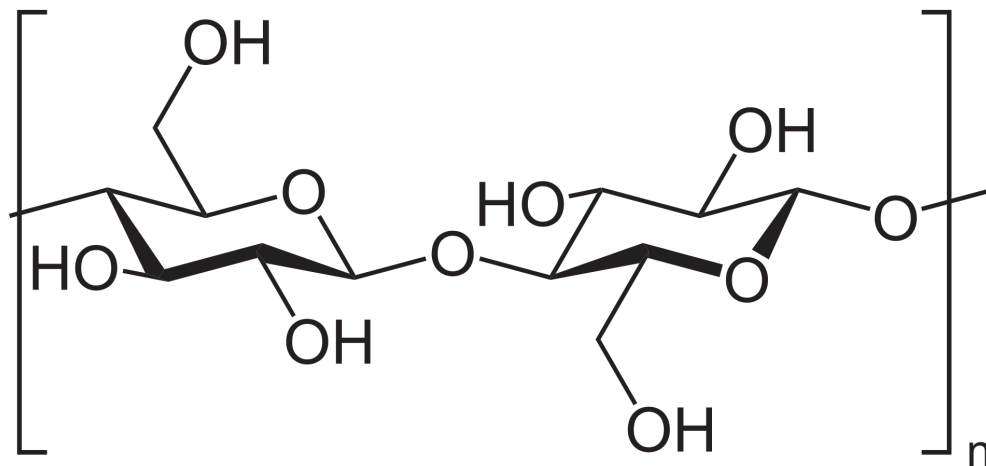
Figure 16: The repeating unit of cellulose. It is made of two anhydroglucose rings linked by an oxygen atom.

chain is composed of more than 10,000 repeating units. However, this length is sufficient to model the chain ends, close to the surface. Many monomers on the real chain do not participate in the adhesion process since long-range non-bonded interactions are negligible for these monomers. Chains of 300 monomers and 100 monomers are analyzed and the properties are found to be similar. Hence, for modeling, 10 chains of 100 monomers are used to simulate the material properties. Additionally, this length is higher than persistent length of these systems.

Five possible structures of cellulose molecules with desired density are created and optimized. Each configuration is subjected to molecular dynamics simulation to let the atoms relax down to the minimum energy in the structure. This model was optimized using a smart algorithm which is a cascade of steepest descent, adjusted basis set Newton-Raphson (ABNR), and quasi-Newton method. Initially, the canonical (NVT) dynamics is carried out
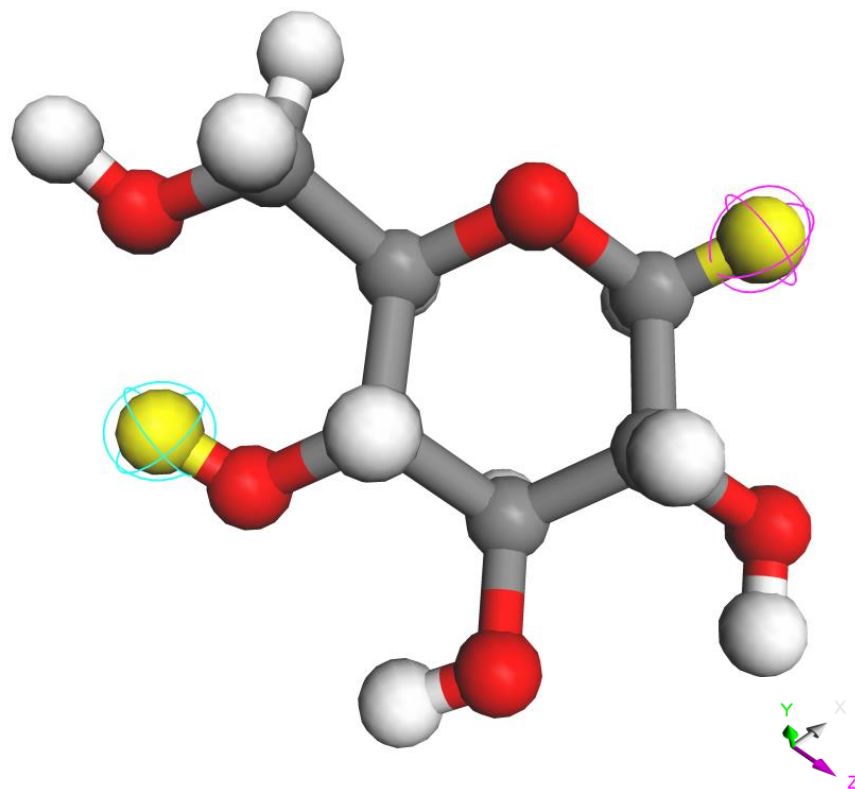
Figure 17: Atomistic models of three different polymer atoms investigated in this study. Gray, red and white represent carbon, oxygen and hydrogen, respectively. The yellow atoms shows where the monomer is connected to the other monomers in the polymers chain. These locations will be replaced by hydrogen at the beginning and at the end of each chain.
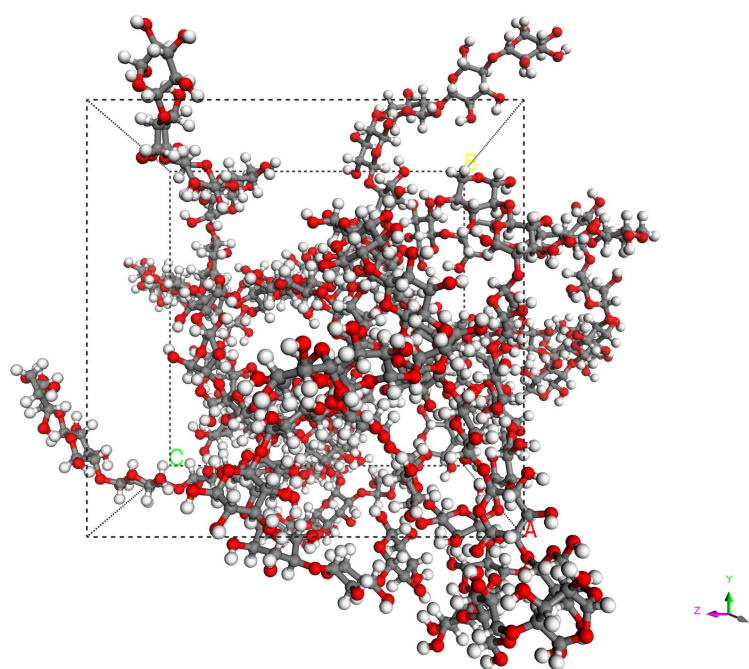
Figure 18: The bulk molecular structure of cellulose model representation in atomistic simulation.

for 80 ps by 0.5 fs time steps at 300 K, followed by the isothermal-isobaric (NPT) dynamics compressed at high pressure (5000 bar) for 120 ps at 300 K. Next, NVT molecular dynamics are applied at 600 K and 300 K, successively, for about 80 ps and 100 ps, respectively. Subsequently, 120 ps molecular dynamics is performed in the NPT ensemble at 1 bar, and the resulting density is compared to the experimental value. If the density is lower than the experimental density, the first two steps are repeated. Finally, molecular dynamics simulation is performed in NVT ensemble at 1 bar for 300 ps.

In order to model the crystalline cellulose, first the unitcell structure is modeled and shown in Fig. 19 and then the whole structure is made by repeating the unitcell.

For both models, the density is found to be 1.6 $\frac{g}{cm^3}$ at 298 K, the Young's modulus of the model is found to be 82 GPa and glass transition temperature found is to be 468 K These numbers are close to the experimental data presented in [63], [64] and [65], respectively.

4.3. SEM/EDX Analysis

In order to investigate the interaction between bamboo fibers and C-S-H, first SEM and EDX analysis were used as it described in the first chapter.

A typical SEM image of a bamboo fiber is shown in Fig. 20.

Moreover, a typical SEM image of a bamboo fiber in the C-S-H matrix is shown in Fig. 21. The image does not show a clear interfacial transition zone between the fibers and cement paste.

The EDX mapping results and analysis for bamboo fiber/cement interfaces are shown in Fig. 22. The X-ray mapping is used to investigate the distribution and density of existing elements such as Si, and Ca in an area
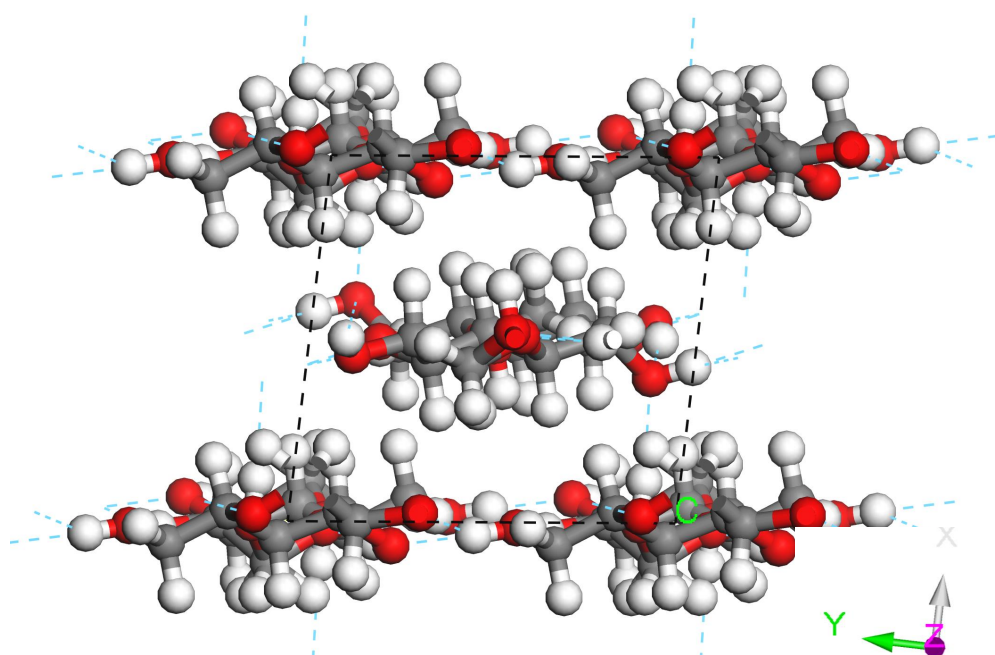
Figure 19: The unitcell structure of modeled crystalline cellulose.
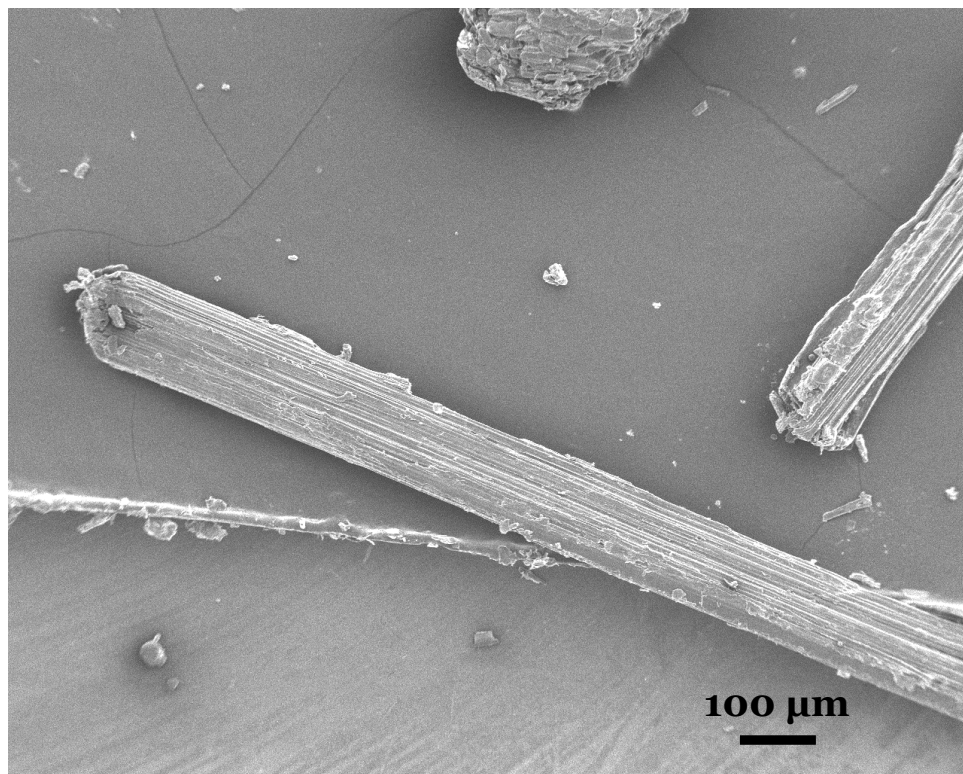
Figure 20: SEM image of the bamboo fibers.
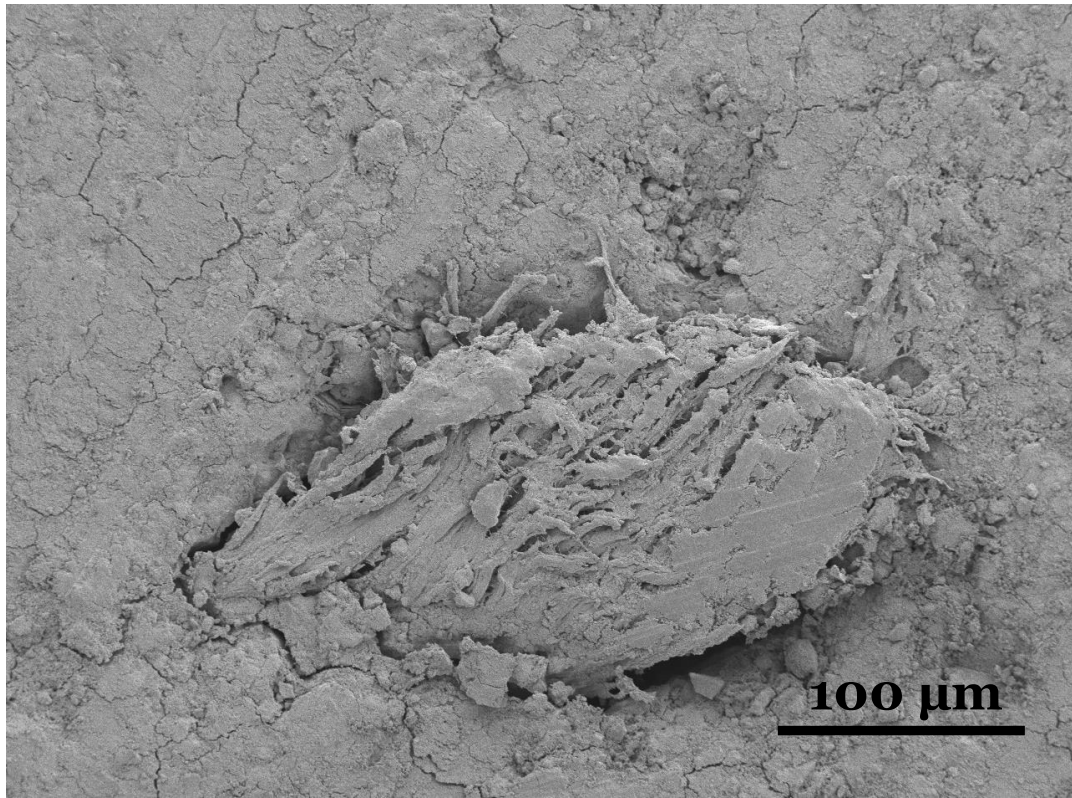
Figure 21: Bamboo fiber in cement paste. There is not a clear interfacial transition zone.

around each fiber. The X-ray mapping of *Si* and *Ca* elements for bamboo fibers show a small accumulation of calcium at fiber/matrix interface, which is represented by an ellipse on the figures. The numerical EDX results in Fig. 23 show that there us a little change in the ratio of C/S in the interfacial zone. The ratio of C/S in the interfacial transition zone between bamboo fibers and cement increases slightly in comparison to the regular C-S-H in fiber-reinforced composite matrices. Molecular modeling is essential in order to obtain a better understanding of the phenomenon.
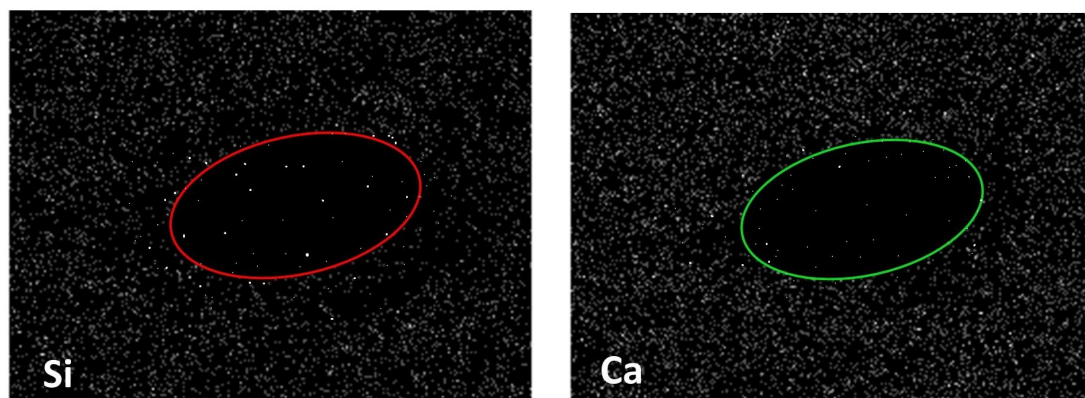
Figure 22: The results of EDX mapping shows the distribution of Ca and Si atoms around bamboo fiber. There is a slight increase in C/S ratio around bamboo fibers.

4.4. Atomic Interaction and Adhesion Energy

The snapshots of the C-S-H/cellulose model before and after the MD simulation are shown in Figs. 24. The binding energies between the C-S-H and cellulose and the concentration profiles of the specific atoms are calculated after the MD simulations.
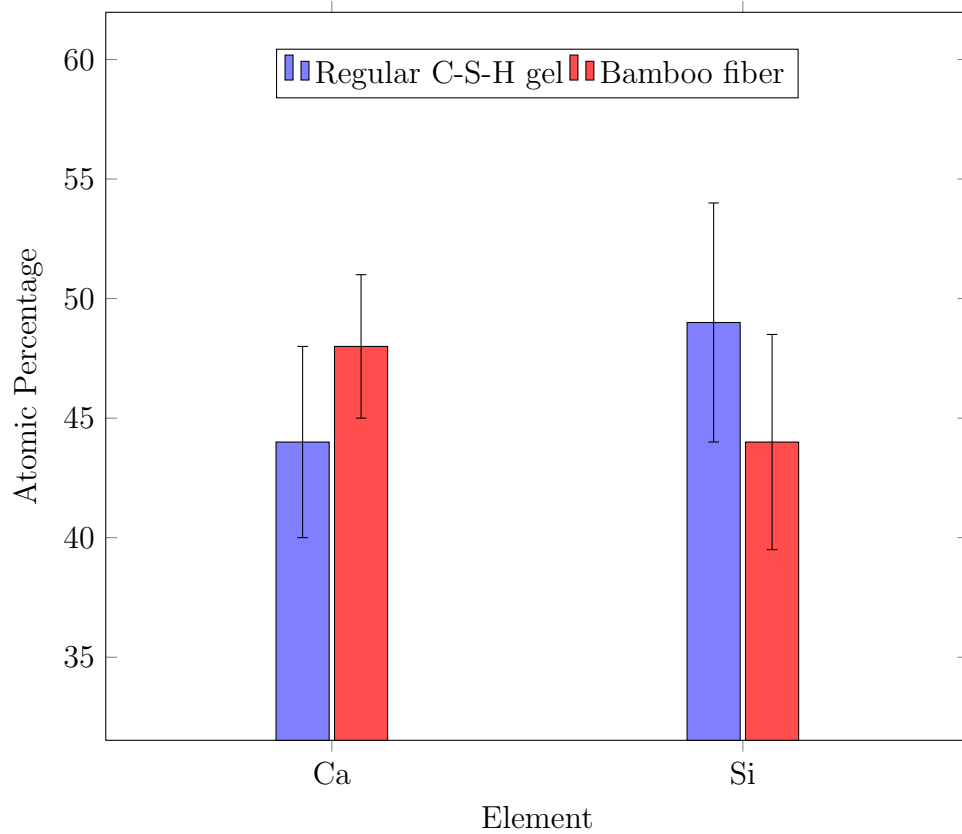
Figure 23: A comparison of the EDX results between atomic percentage of *Ca* and *Si* elements on samples of regular C-S-H gels and EDX results on samples of bamboo fiber/C-S-H gel interfaces. Ten EDX spectra are used for each sample.
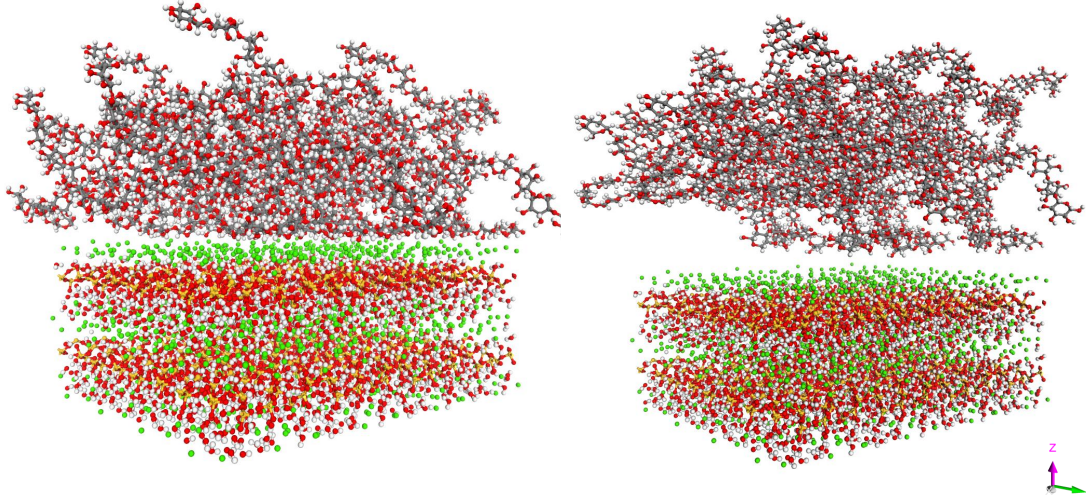
Figure 24: The nanostructure of noncrystalline cellulose/C-S-H interface before, (right), and after simulation (left).

The interaction energy ($E_{Interaction}$) between the molecules and the C-S-H surface is calculated by using the Equation 7. Now, $E_{Interaction}$ is the interaction energy of the system. E_{total} is the total energy of the C-S-H surface and the cellulose molecules in equilibrium. E_{C-S-H} is the energy of the surface alone, and $E_{polymer}$ is the energy of the cellulose without the surface, both separated in vacuum in equilibrium [43]. These calculations are all single point energies with no constraints defined in the model.

As it was mentioned before, most of the wood cellulose is crystalline. Hence, cellulose with crystal structure is made and the interaction energy was investigated. Since, there is a difference between different planes of cellulose, there may be a difference in the interaction between different surfaces and C-S-H structure. In this study we simulated the interaction between crystalline

47

cellulose on [00-1] and [010] and C-S-H structure. The Figs. 25 and 26 show the cellulose/C-S-H interface before and after MD simulations.
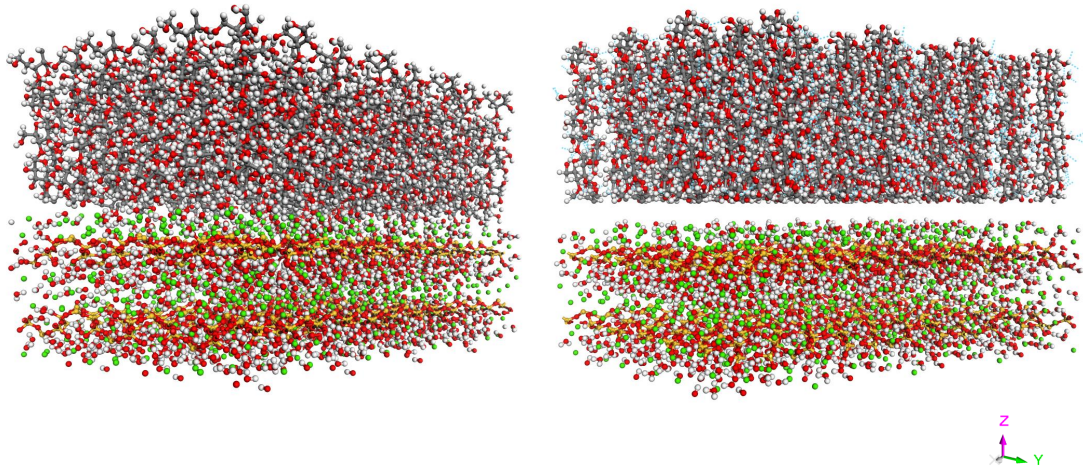
Figure 25: The nanostructure of crystalline [00-1] cellulose/C-S-H interface before, (right), and after simulation (left).

Fig. 27 shows the possibility of forming hydrogen bond between and inside the molecules of cellulose. These hydrogen bonds are responsible for the high strength of cellulose. Since these hydrogen bonds are very strong there is no polar group to contribute to the adhesion of cellulose with C-S-H gel. Therefore the adhesion would be lower than that of the other three polymers.

In the bamboo fiber-reinforced cement paste samples it was observed that the samples are pretty dry which means bamboo fibers absorbed a lot of water during hydration reaction. Moreover, it is known that water play a very important role in the properties of biomaterials. Hence, water was
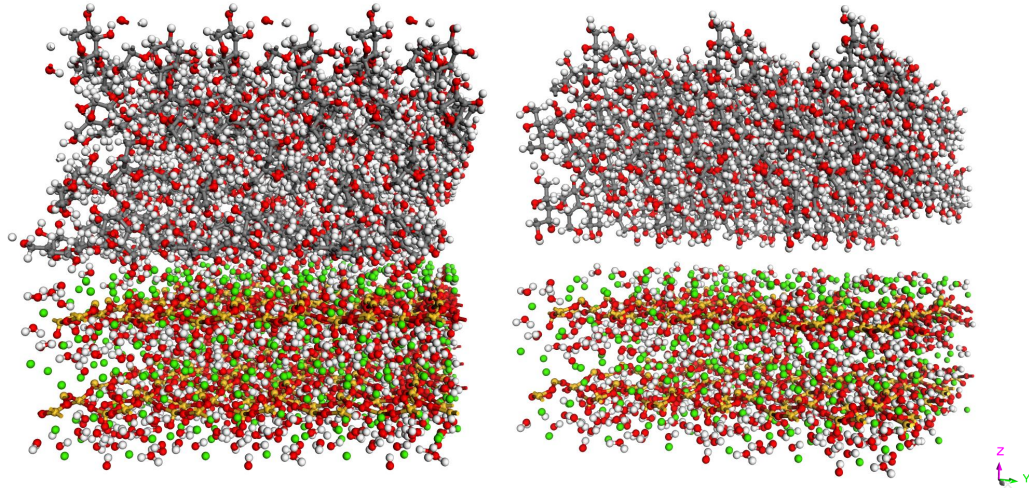
Figure 26: The nanostructure of crystalline [010] cellulose/C-S-H interface before, (right), and after simulation (left).

added to the structure of cellulose and adhesion energy was calculated again. A summery of the simulations are presented in Table 5.

Table 5: The total adhesion energies ($\frac{J}{m^2}$) of amorphous and two crystalline structure of cellulose with C-S-H gel.

	Without Water			With Water		
	Amorphous	[00-1]	[010]	Amorphous	[00-1]	[010]
Adhesion	39.2	8.6	21.1	85.8	8.1	20.5
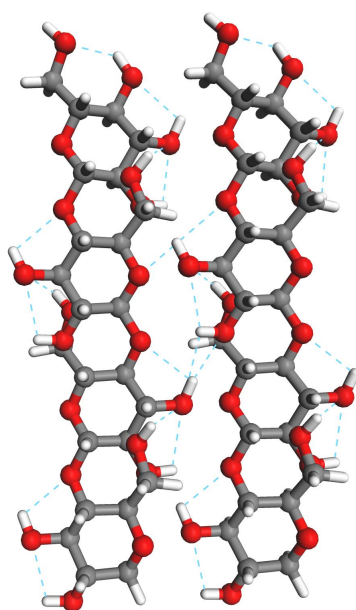
Figure 27: The hydrogen bond formation in cellulose. Dot blue lines show the H-bond between and in the molecules of cellulose.

5. Chapter 5: Mechanical Testing

The tensile strength of concrete is a very important parameter in the design of civil engineering structures. In order to determine the tensile strength of concrete for existing structures, different experiments are essential. Compression tests are very common in order to investigate the compressive strength of concrete and fiber-reinforced concrete samples. Because of the complex nature of uniaxial tension tests, usually splitting tension tests are carried out on cylindrical specimens or cores. In this study, split testing setup was chosen because of the fiber-pullout effect on the polymeric fibers which is affected by the adhesion energies.

5.1. Materials and Methods

Here, samples preparation and mechanical testing set-up will be explained.

5.1.1. Samples Preparation

In order to compare the mechanical properties of fiber-reinforce cement paste and investigating the effect of different polymeric fibers in concrete and their molecular level interaction, concrete samples were prepared. For all the samples, first, 40 % mass percentage is water and the rest is cement. For samples with polymeric fibers, 1 % volume percentage is added to the mixtures. Nine samples of each control, cement/PVA, cement/Nylon and Cement/Polypropylene batches are prepared. Three of each batch are tested in third day, Three in the seventh day and Three in the twenty first day. The fibers shape is identical. $\frac{3}{4}$ in long and 175 μm thick polymeric fibers were used.

5.1.2. Split-cylinder Test

Split-cylinder test is the indirect way to determine tensile strength of the concrete samples. This test was chosen in order to investigate the effect of adhesion energy between fiber and cement paste. In this test, a standard test cylinder (4 in long and 2 in diameter) was placed horizontally between the loading surfaces of compression test machine. With this method, load is applied uniformly along the length of the samples and cause a crack along the diameter of the cylinder. The sample split into two parts due to the Poisson's effect. If an element on the diameter of the sample is assumed, in addition to a pair of compression load, a pair of tension load is applied to the element perpendicular to the loading direction.

Assuming an elastic behavior for the concrete, the tensile stress acting on the vertical plane on the diameter of the cylinder can be calculated as:

$$\sigma = \frac{2P}{\pi DL} \tag{8}$$

where P is the compression force, D is the diameter of the cylinder and L is the length of cylinder.

5.2. Results and Discussion

A typical broken sample after split-cylinder test is shown in Fig. 28. The long fibers can be observed in the image. From this image, three main failure steps are implied: failure of concrete, fiber detachment or debonding and fiber pull-out continuation. The first one occurs at the failure tensile strength of concrete, the second one is when the stress in the sample exceed the adhesion force per area between fibers and concrete and the third step occurs due to the friction between fibers and concrete.

Figure 28: A typical broken fiber-reinforce cement paste sample subjected to split-cylinder test.

Failure strength of fiber-reinforced cement paste can be obtained from testing control samples. A typical load-displacement graph of a cement paste sample with no additive and a sample with polymeric fiber is shown in Fig. 29. In the samples with fibers, the last step of failure strongly depends on the roughness of the fibers in nano and micro scale. However, there is a correlation between the second step of failure and the adhesion energies found in the previous chapters. The force corresponds to this point is called yielding load in this study.
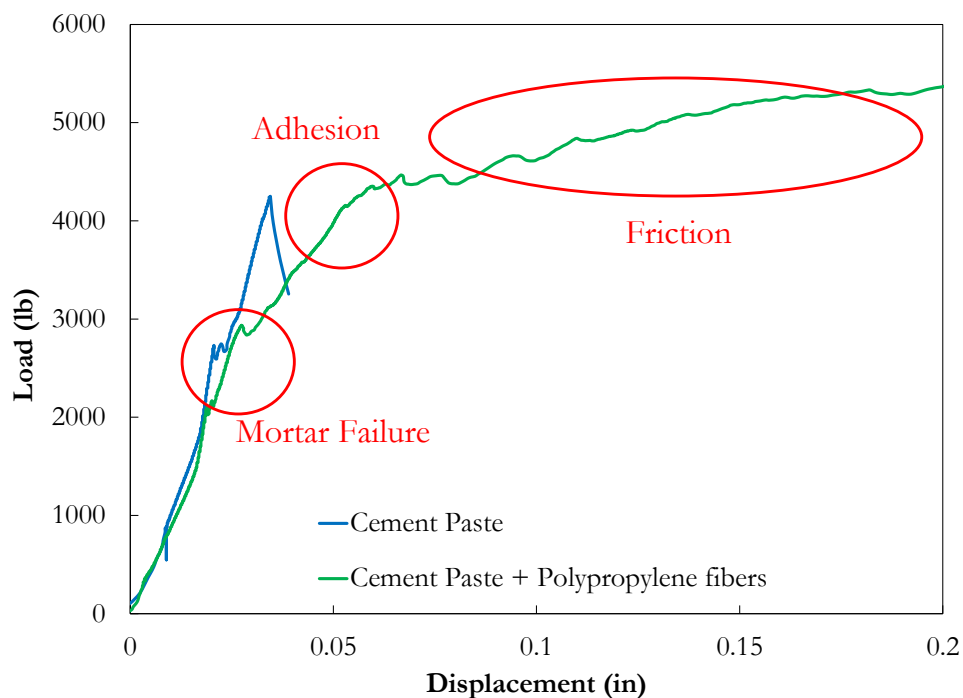
Figure 29: Typical failure of cement paste and fiber-reinforced cement paste.

Figs. 30-32 show the load-displacement behavior of tested samples in the

third day. The circles on the graphs show the second step of failure. The load corresponds to this part is higher for Cement/Nylon samples than for Cement/PVA samples, and it is higher for Cement/PVA samples than for Cement/Polypropylene samples.
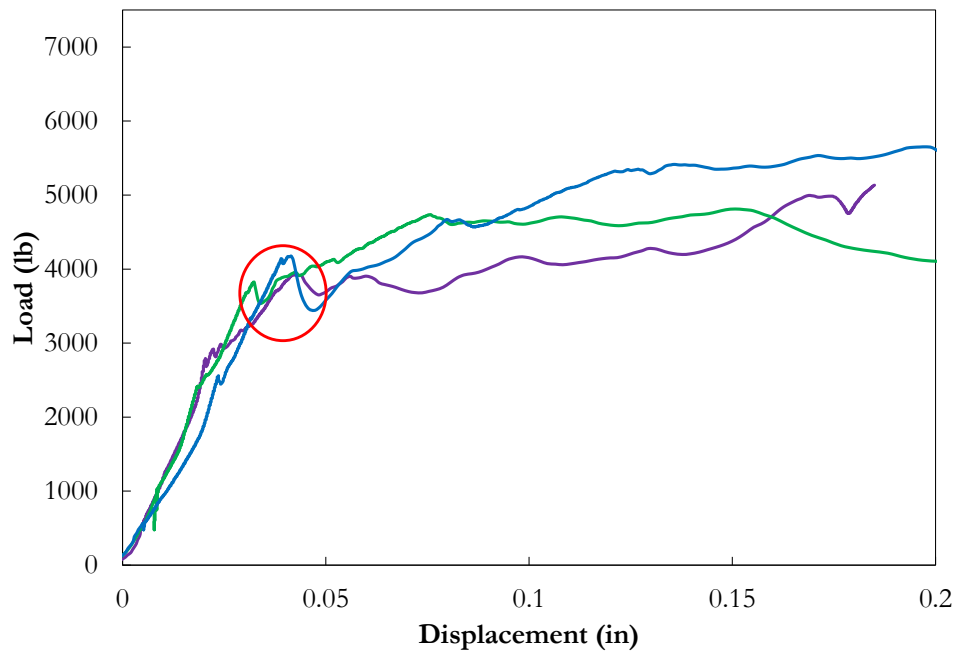
Figure 30: Load-displacement curve for cement paste with added Polypropylene fibers cured for three days. The yielding load is around 4000 lb.

The following graphs show the tested samples for seventh and twenty-eighth days. The same trend for the yielding stress can be observed in the samples.

The yielding stress for samples with PVA and Polypropylene are pretty
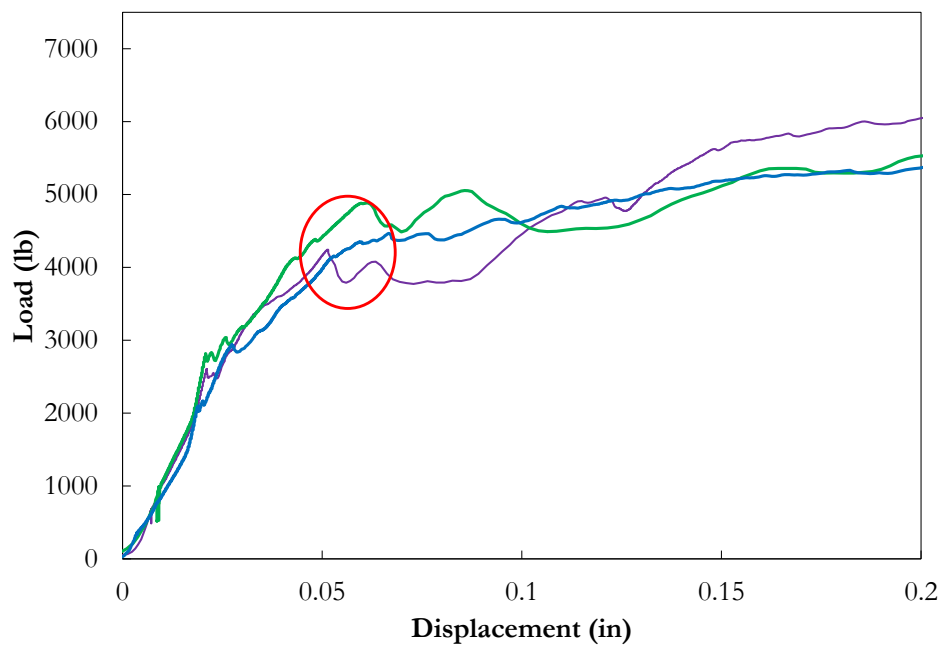
Figure 31: Load-displacement curve for cement paste with added PVA fibers cured for three days. The yielding load is around 4200 lb.
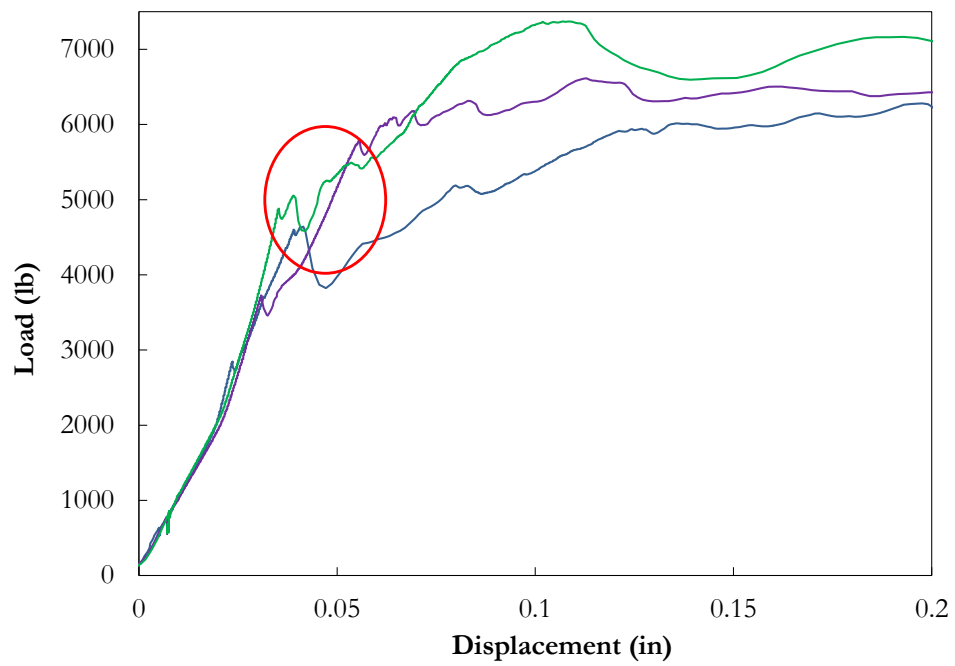
Figure 32: Load-displacement curve for cement paste with added Nylon fibers cured for three days. The yielding load is around 5000 lb.
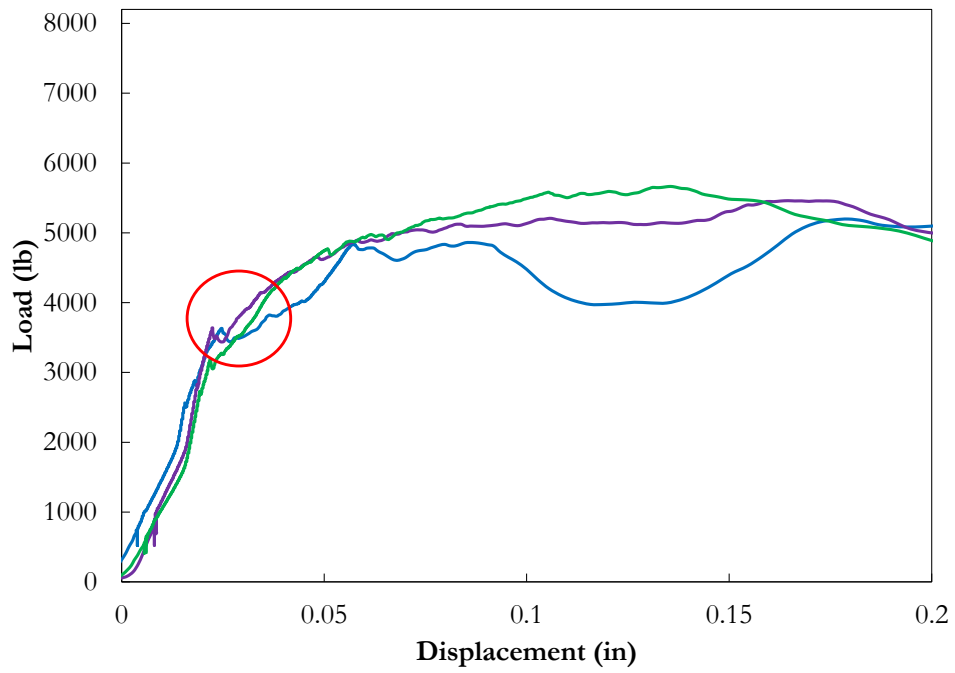
Figure 33: Load-displacement curve for cement paste with added Polypropylene fibers cured for seven days. The yielding load is around 3900 lb.
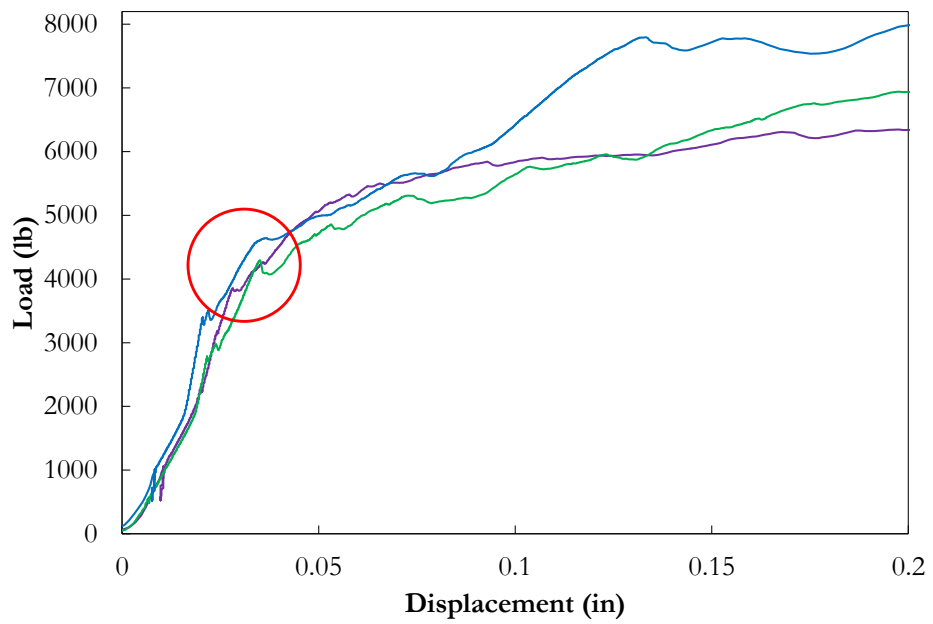
Figure 34: Load-displacement curve for cement paste with added PVA fibers cured for seven days. The yielding load is around 4200 lb.
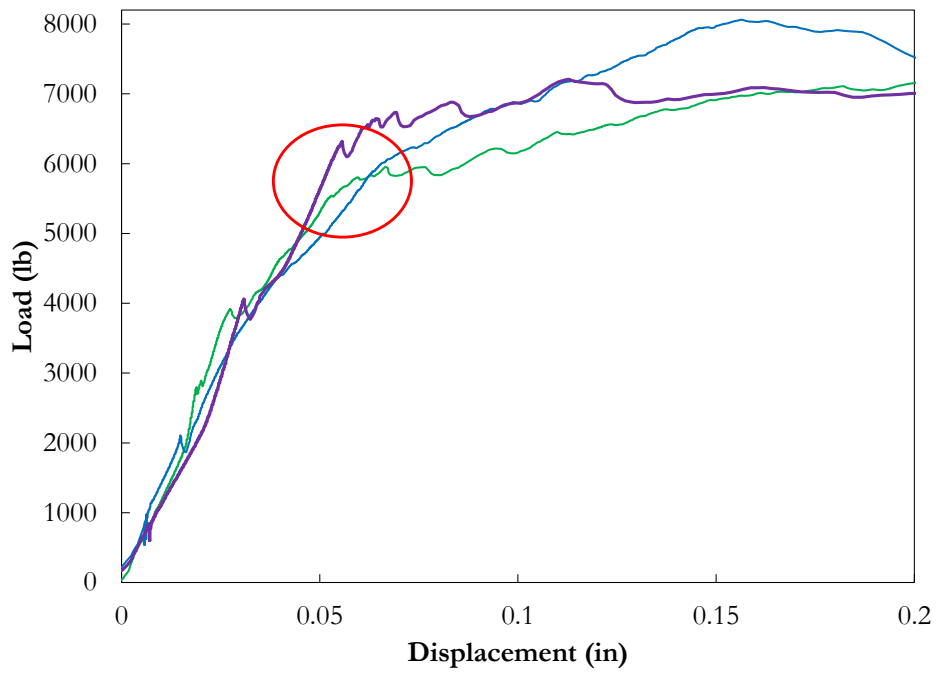
Figure 35: Load-displacement curve for cement paste with added Nylon fibers cured for seven days. The yielding load is around 5800 lb.
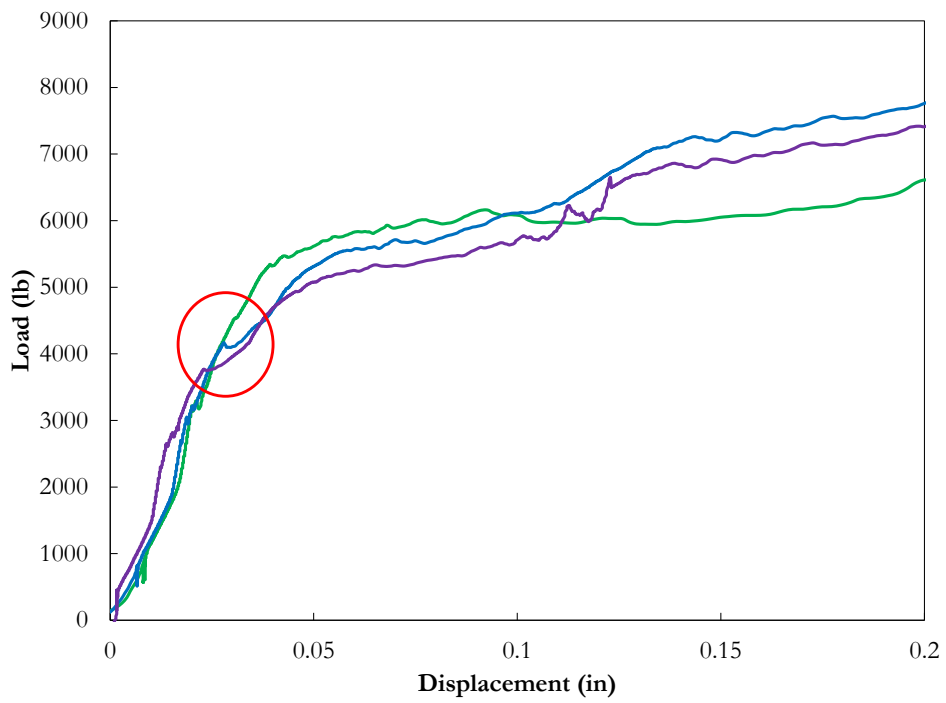
Figure 36: Load-displacement curve for cement paste with added Polypropylene fibers cured for twenty eight days. The yielding load is around 3900 lb.
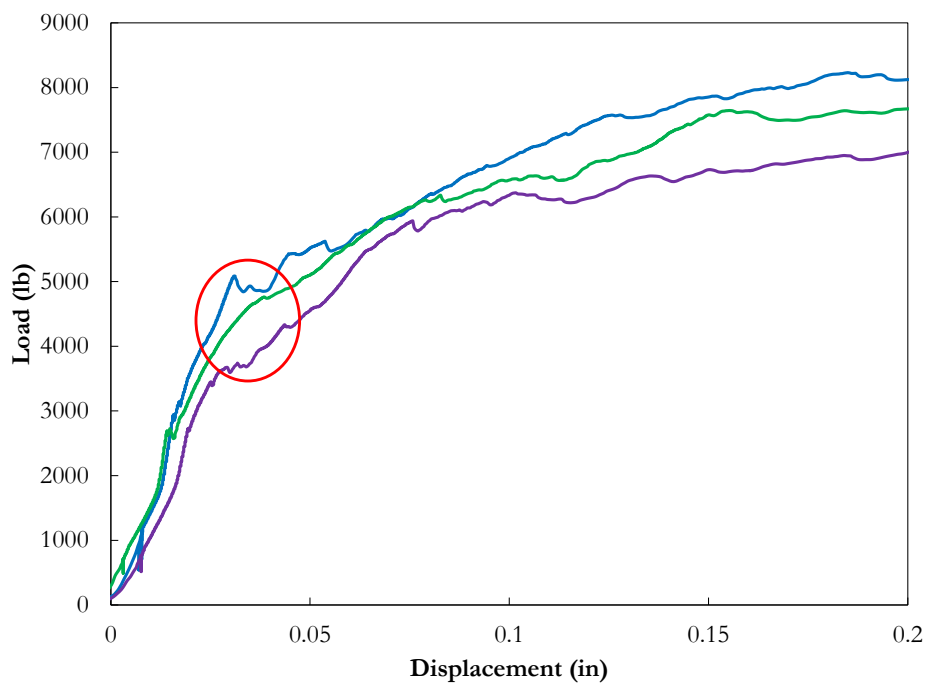
Figure 37: Load-displacement curve for cement paste with added PVA fibers cured for twenty eight days. The yielding load is around 4100 lb.
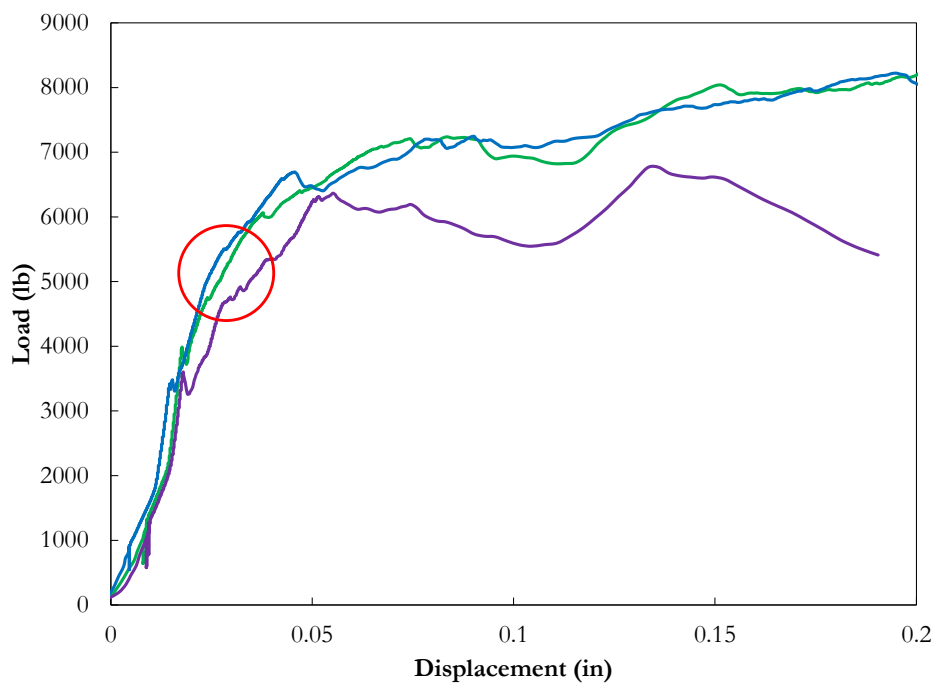
Figure 38: Load-displacement curve for cement paste with added Nylon fibers cured for twenty eight days. The yielding load is around 5000 lb.
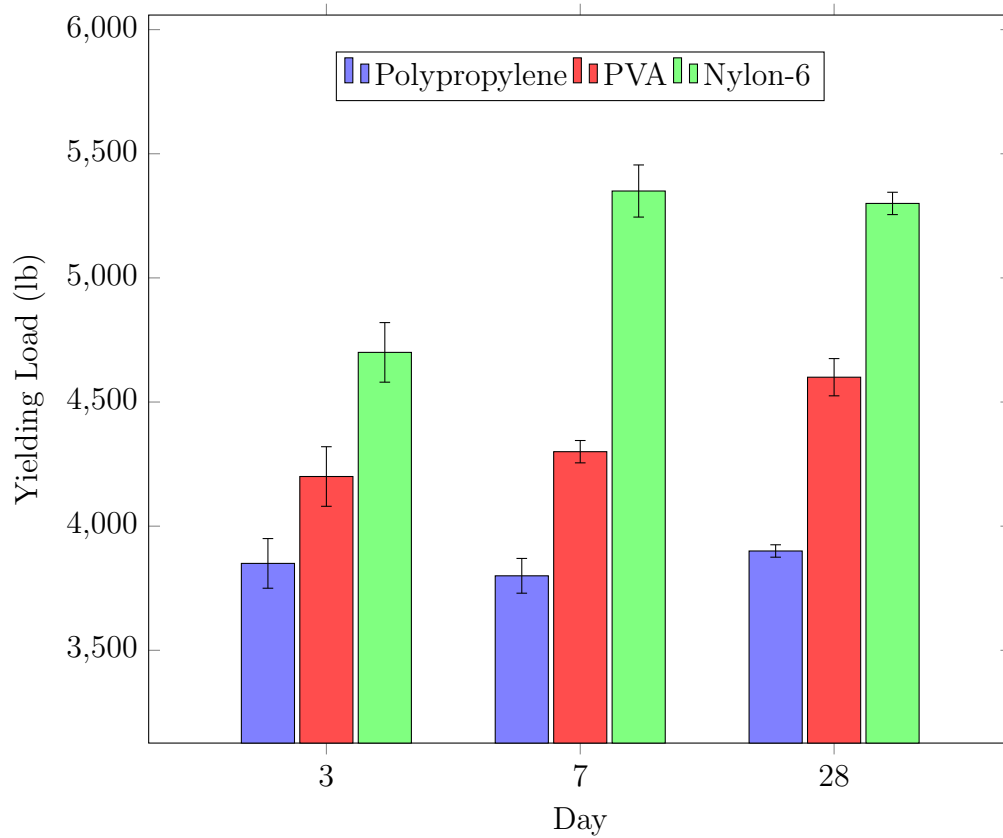
Figure 39: Summery of the split-cylinder test results.

close, however, the stress for samples with Nylon fibers is higher. To conclude the graphs can be summerized in the graph below:

6. Conclusion and Future works

Across the globe, polymer fibers are added to concrete to enhance the tensile properties and ductility of concrete. While there is a large body of data on this subject, the nanostructure and nanomechanical properties of the polymer fiber/cement interface is still not completely known which is pivotal in the design of robust polymer reinforced concrete. This study presents a combined SEM/EDX analysis and atomistic simulation framework to investigate the nanostructure of the cement/fiber interfaces, and the corresponding mechanical properties. In this study, different polymer fibers are used based on different polarity of their functional group. The electron microscopy results show that the ratio of C/S changes in the fiber/matrix interface for the three types of polymer fibers studied. This is essentially due to the different polarities of the polymer molecules. Using SEM/EDX analysis, it is shown that the C/S ratios in PVA/C-S-H and nylon-6/C-S-H interfaces are higher than that in polypropylene/C-S-H interface. This is mainly a result of high polarity of hydroxyl and amide functional groups. In order to further investigate this hypothesis, using the proposed atomistic model, the adhesion energies between different polymers and C-S-H are computed. It is observed that the functional group affects the adhesion energy primarily by changing the C/S ratio of the C-S-H at the interface, and further, by absorbing additional positive ions in the C-S-H structure.

In chapter 1, it is explained how SEM/EDX analysis can be used to investigate the fiber/matrix interface in fiber-reinfoced concrete. The results show that there is a change in C/S ratio in fiber/matrix interface rather than the regular C-S-H.

In chapter 2 and 3, basic principals of molecular modeling of polymers and C-S-H were presented. The results of chapter 1 were used to change the atomic structure of C-S-H in the interface and investigate the molecular interaction between C-S-H and polymeric fibers.

In chapter 4, bamboo fibers were added to cement paste and their effect on the interface and molecular structure of C-S-H were investigated. Both SEM/EDX technique and Molecular modeling was used in this chapter.

In chapter 5, mechanical testing was performed on samples and a correlation between adhesion energies and load-displacement curves were found. The split-cylinder test was used to investigate the macroscopic behaviour of samples and the results were compared to the molecular interaction between C-S-H and polymers. We believe that the adhesion energy between fibers and cement paste can be correlated with the fiber detachment in load-displacement curves.

The implications of these results are significant in further development of robust fiber reinforced cement composites. Future work will focus on understanding the rate of migration of calcium atoms at the surface/interface, the more investigation of the effect of adhesion energies on mechanical response of fiber-reinforced cement composites.

[1] Balaguru PN, Shah SP. *Fiber-reinforced cement composites.* 1992.

[2] Sakulich AR. Reinforced geopolymer composites for enhanced material greenness and durability. *Sustainable cities and society.* 2011;1: 195-210.

[3] Sharifi NP, Sakulich A. Application of Phase Change Materials in Structures and Pavements. *Proceedings of the 2nd International Workshop on Design in Civil and Environmental Engineering: Mary Kathryn Thompson*, 2013:82.

[4] Sharifi NP, Sakulich A. Application of phase change materials to improve the thermal performance of cementitious material. *Energy and Buildings.* 2015;103: 83-95.

[5] Akihama S, Suenaga T, Nakagawa H, Suzuki K. Experimental Study of Vinylon Fiber Reinforced Cement Composites. VFRC"(Part I). *Kajima Annual Technical Report*, Kajima Corporation. 1985;33: 123-128.

[6] Garcia S, Naaman AE, Pera J. Experimental investigation on the potential use of poly (vinyl alcohol) short fibers in fiber-reinforced cement-based composites. *Materials and Structures.* 1997;30: 43-52.

[7] Betterman L, Ouyang C, Shah S. Fiber-matrix interaction in microfiber-reinforced mortar. *Advanced cement based materials.* 1995;2: 53-61.

[8] Li VC, Chan Y-W, Wu H-C. *Interface strengthening mechanisms in polymeric fiber reinforced cementitious composites* 1994.

[9] Global Cement Report (International Cement Review, London, ed. 9, 2011).

[10] Van Vliet K, Pellenq R, Buehler MJ, et al. Set in stone? A perspective on the concrete sustainability challenge.*MRS bulletin.* 2012;37: 395-402.

[11] Bentur A, Mindess S. Fibre reinforced cementitious composites. *CRC Press*, 2006.

[12] Sakulich AR, Li VC. Nanoscale characterization of engineered cementitious composites (ECC). *Cement and Concrete research.* 2011;41: 169-175.

[13] Dolado JS, Griebel M, Hamaekers J. A molecular dynamic study of cementitious calcium silicate hydrate (CSH) gels. *Journal of the American Ceramic Society.* 2007;90: 3938-3942.

[14] Yu P, Kirkpatrick RJ, Poe B, McMillan PF, Cong X. Structure of calcium silicate hydrate (C-S-H): Near-, Mid-, and Far-infrared spectroscopy. *Journal of the American Ceramic Society.* 1999;82: 742-748.

[15] Soyer-Uzun S, Chae SR, Benmore CJ, Wenk HR, Monteiro PJ. Compositional evolution of calcium silicate hydrate (CSH) structures by total x-ray scattering. *Journal of the American Ceramic Society.* 2012;95: 793-798.

[16] Allen AJ, Thomas JJ, Jennings HM. Composition and density of nanoscale calciumsilicatehydrate in cement. *Nature materials.* 2007;6: 311-316.

[17] Hamid S. The crystal structure of the 11 natural tobermorite Ca2. 25 [Si3O7. 5 (OH) 1.5] 1H2O. *Zeitschrift fr Kristallographie-Crystalline Materials.* 1981;154: 189-198.

[18] Taylor H. Nanostructure of C- S- H: Current status. *Advanced cement based materials.* 1993;1: 38-46.

[19] Shahsavari R, Pellenq RJ-M, Ulm F-J. Empirical force fields for complex hydrated calcio-silicate layered materials. *Physical Chemistry Chemical Physics.* 2011;13: 1002-1011.

[20] Pellenq R-M, Lequeux N, Van Damme H. Engineering the bonding scheme in CSH: The iono-covalent framework. *Cement and Concrete research.* 2008;38: 159-174.

[21] Richardson I. The calcium silicate hydrates. *Cement and Concrete research.* 2008;38: 137-158.

[22] Wu W, Al-Ostaz A, Cheng AH-D, Song CR. Computation of elastic properties of Portland cement using molecular dynamics. *Journal of Nanomechanics and Micromechanics.* 2011;1: 84-90.

[23] Richardson I. Tobermorite/jennite-and tobermorite/calcium hydroxide-based models for the structure of CSH: applicability to hardened pastes of tricalcium silicate, -dicalcium silicate, Portland cement, and blends of Portland cement with blast-furnace slag, metakaolin, or silica fume. *Cement and Concrete research.* 2004;34: 1733-1777.

[24] Bauchy M, Qomi MA, Ulm F-J, Pellenq R-M. Order and disorder in calciumsilicatehydrate. *The Journal of Chemical Physics.* 2014;140: 214503.

[25] Pellenq RJ-M, Kushima A, Shahsavari R, et al. A realistic molecular

model of cement hydrates. *Proceedings of the National Academy of Sciences.* 2009;106: 16102-16107.

[26] Qomi MA, Krakowiak K, Bauchy M, et al. Combinatorial molecular optimization of cement hydrates. *Nature communications.* 2014;5.

[27] Verlet L. Computer" experiments" on classical fluids. I. Thermodynamical properties of Lennard-Jones molecules. *Physical review.* 1967;159: 98.

[28] McNaught AD, McNaught AD. Compendium of chemical terminology. *Blackwell Science Oxford,* 1997.

[29] Sun H. COMPASS: an ab initio force-field optimized for condensed-phase applications overview with details on alkane and benzene compounds. *The Journal of Physical Chemistry B.* 1998;102: 7338-7364.

[30] Sun H, Ren P, Fried J. The COMPASS force field: parameterization and validation for phosphazenes. *Computational and Theoretical Polymer Science.* 1998;8: 229-246.

[31] Grujicic M, Sun Y-P, Koudela K. The effect of covalent functionalization of carbon nanotube reinforcements on the atomic-level mechanical properties of poly-vinyl-ester-epoxy. *Applied Surface Science.* 2007;253: 3009-3021.

[32] Lu Z, Dunn ML. van der Waals adhesion of graphene membranes. *Journal of Applied Physics.* 2010;107: 044301.

[33] Rappe AK, Goddard III WA. Charge equilibration for molecular dynamics simulations. *The Journal of Physical Chemistry.* 1991;95: 3358-3363.

[34] Manzano H, Dolado J, Ayuela A. Elastic properties of the main species present in Portland cement pastes. *Acta Materialia.* 2009;57: 1666-1674.

[35] Manzano H, Dolado J, Guerrero A, Ayuela A. Mechanical properties of crystalline calcium-silicate-hydrates: comparison with cementitious C-S-H gels. *physica status solidi (a).* 2007;204: 1775-1780.

[36] Constantinides G, Ulm F-J. The effect of two types of CSH on the elasticity of cement-based materials: Results from nanoindentation and micromechanical modeling. *Cement and Concrete research.* 2004;34: 67-80.

[37] Gujrati PD, Leonov AI. Modeling and Simulation in Polymers. *John Wiley & Sons,* 2010.

[38] Cranford SW, Ortiz C, Buehler MJ. Mechanomutable properties of a PAA/PAH polyelectrolyte complex: rate dependence and ionization effects on tunable adhesion strength.*Soft Matter.* 2010;6: 4175-4188.

[39] Hossain D, Tschopp M, Ward D, Bouvard J, Wang P, Horstemeyer M. Molecular dynamics simulations of deformation mechanisms of amorphous polyethylene.*Polymer.* 2010;51: 6071-6083.

[40] Debenedetti PG, Stillinger FH. Supercooled liquids and the glass transition. *Nature.* 2001;410: 259-267.

[41] Capaldi FM, Boyce MC, Rutledge GC. Molecular response of a glassy polymer to active deformation. *Polymer.* 2004;45: 1391-1399.

[42] Lequeux N, Morau A, Philippot S, Boch P. Extended X-ray Absorption Fine Structure Investigation of Calcium Silicate Hydrates. *Journal of the American Ceramic Society.* 1999;82: 1299-1306.

[43] Kisin S, Bozovic Vukic J, van der Varst PGT, de With G, Koning CE. Estimating the polymer-metal work of adhesion from molecular dynamics simulations. *Chemistry of materials.* 2007;19: 903-907.

[44] Askeland DR, Phul PP. *The science and engineering of materials* 2003.

[45] Rachtanapun P, Selke SE, Matuana LM. Relationship between cell morphology and impact strength of microcellular foamed high-density polyethylene/polypropylene blends. *Polymer Engineering & Science.* 2004;44: 1551-1560.

[46] Liu H, Wu Q, Zhang Q. Preparation and properties of banana fiber-reinforced composites based on high density polyethylene (HDPE)/Nylon-6 blends.*Bioresource technology.* 2009;100: 6088-6097.

[47] Pakzad A, Simonsen J, Yassar RS. Elastic properties of thin poly (vinyl alcohol)cellulose nanocrystal membranes. *Nanotechnology.* 2012;23: 085706.

[48] Svoboda P, Theravalappil R, Svobodova D, et al. Elastic properties of polypropylene/ethyleneoctene copolymer blends. *Polymer Testing.* 2010;29: 742-748.

[49] Fornes T, Yoon P, Keskkula H, Paul D. Nylon 6 nanocomposites: the effect of matrix molecular weight. *Polymer.* 2001;42: 09929-09940.

[50] Liu T, Phang IY, Shen L, Chow SY, Zhang W-D. Morphology and mechanical properties of multiwalled carbon nanotubes reinforced nylon-6 composites. *Macromolecules.* 2004;37: 7214-7222.

[51] Finch CA. Polyvinyl alcohol: developments.*Wiley,* 1992.

[52] Samir, M. A. S. A.; Alloin, F.; Dufresne, A. *Biomacromolecules* 2005, 6, 612626.

[53] Berglund, L. A.; Peijs, T. *MRS Bull.* 2010, 35, 201207

[54] Matthews, J. F.; Scopec, C. E.; Mason, P. E.; Zuccato, P.; Torget, R. W.; Sugiyama, J.; Himmel, M. E.; Brady, J. W. Carbohydr. *Res.* 2006, 341, 138152.

[55] Bergenstrale, M.; Berglund, L. A.; Mazeau, K. *J. Phys. Chem. B* 2007, 111, 91389145.

[56] Mazeau, K.; Rivet, A. Biomacromolecules 2008, 9, 13521354.

[57] Zhong, L.; Matthews, J. F.; Crowley, M. F.; Rignall, T.; Talon, C.; Cleary, J. M.; Walker, R. C.; Chukkapalli, G.; McCabe, C.; Nimlos, M. R.; C., L. B., III; Himmel, M. E.; Brady, *J. W. Cellulose* 2008, 15, 261273.

[58] Nishiyama, Y.; Johnson, G. P.; French, A. D.; Forsyth, V. T.; Langan, P. *Biomacromolecules* 2008, 9, 31333140.

[59] Lins, R. D.; Hunenberger, P. H. *J. Comput. Chem.* 2005, 26, 14001412.

[60] Guvench, O.; Greene, S. N.; Kamath, G.; Brady, J. W.; Venable, R. M.; Pastor, R. W.; MacKerell, A. D., Jr. *J. Comput. Chem.* 2008, 29, 25432564.

[61] Sun, H.; Mumby, S. J.; Maple, J. R.; Hagler, A. T. *J. Am. Chem. Soc.* 1994, 116, 29782987.

[62] Kirschner, K. N.; Yongye, A. B.; Tschampel, S. M.; Gonzalez Outeirino, J.; Daniels, C. R.; Foley, B. L.; Woods, R. J. *J. Comput. Chem.* 2007, 29, 622655

[63] Sun, C. C. (2005). True density of microcrystalline cellulose. *Journal of pharmaceutical sciences*, 94(10), 2132-2134.

[64] Nishino, T., Takano, K., & Nakamae, K. (1995). Elastic modulus of the crystalline regions of cellulose polymorphs. *Journal of Polymer Science Part B: Polymer Physics,* 33(11), 1647-1651.

[65] Szczeniak, L., Rachocki, A., & Tritt-Goc, J. (2008). Glass transition temperature and thermal decomposition of cellulose powder. *Cellulose*, 15(3), 445-451.